Electric Field Induced Second Harmonic (EFISH) measurements of highly boron doped p^+-type Si/SiO$_2$

by

Pieter Herman Neethling

Dissertation presented for the degree

Doctor of Philosophy

at the University of Stellenbosch

Supervisor:
Prof. E.G. Rohwer
Co-supervisor:
Prof. H.M. von Bergmann

August 2008

Declaration

I, the undersigned, hereby declare that the work contained in this thesis is my own original work and that I have not previously in its entirety or in part submitted it at any university for a degree.

....

Signature

28 / 08 / 2008

....

Date

Abstract

The advent of high intensity short pulse lasers has opened the door to investigating buried solid-solid interfaces through the technique of optical second harmonic generation (SHG). This has led to extensive study of technologically important systems such as the Si/SiO_2 interface. In this study, SHG is employed to study the interface between highly boron doped p^+-type Si and its native oxide layer (SiO_2).

Previous studies from this laboratory have extensively investigated the photo-induced charge transfer process across the Si/SiO_2 interface in the case of undoped natively oxidized Si by means of SHG, with initial SHG measurements being performed on boron doped p^+-type Si.

The natively oxidized p^+-type Si/SiO_2 sample was placed on a computer controlled positioning system which allowed for translation of the sample and rotation around the azimuth. The laser system employed was characterized in terms of spectral composition, pulse duration, pulse repetition rate, spatial profile and pulse energy in order to ensure quantitative measurements. The SHG signal generated from the sample interface was recorded in reflection.

Under the applied irradiation conditions, defects are created at the interface by the near infra red (NIR) femtosecond radiation from the laser. These defects are then populated via multi-photon processes by electrons and to a lesser extent holes. The charge transfer across the interface induces an interfacial electric field. This photo-induced electric field is in addition to the built-in interfacial electric field caused by positive ionization of naturally occurring interfacial defects due to the strong doping of the bulk Si.

It is this interfacial electric field, consisting of the built-in doping induced field and the photo-induced electron and hole fields, that is probed by SHG. The SHG signal is strongly dependent on the magnitude of this interfacial electric field as the electric field induced second harmonic (EFISH) signal dominates all other contributions to the observed SHG signal in the case of the Si/SiO_2 system.

The temporal evolution of the SHG signal is recorded for different intensities from virgin as well as the pre-irradiated samples. This yields information about the time scales on which the charge separation occurs as well as the influence of existing photo-induced trap sites on the charge separation process, since the strength of the SHG signal is an indirect measure of the interfacial electric field strength. The angular dependence of the SHG signal (SH rotational anisotropy measurements) for both the initial signal (when the doping induced electric field dominates) and the saturated signal (when the electron induced electric field dominates) is measured. Both these measurements show a four fold symmetry but with a relative 45° phase shift between them. This

is taken as confirmation of the reversal of the interfacial electric field direction. The initial SHG signal as a function of intensity is also recorded for different incident wavelengths. The variation in the non-quadratic dependence of the initial SHG signal on the incident intensity is attributed to a resonant enhancement of two-photon absorption and subsequent screening of the interfacial electric field by charge carriers.

The measurement performed and the results obtained contribute to the understanding of the photo-induced charge separation process across buried solid-solid interfaces, specifically as it applies to the important Si/SiO_2 interface.

Opsomming

Die beskikbaarheid van ultrakortpuls lasers, en die gepaardgaande hoë intensiteite wat die lasers kan genereer, het die ondersoek van die tussenvlak tussen twee vastestowwe deur middel van optiese tweede harmoniek opwekking (THO) toeganklik gemaak. Dit het gelei tot ondersoeke van tegnologies belangrike sisteme soos die Si/SiO_2 tussenvlak. Hierdie studie fokus op die ondersoek van die tussenvlak tussen p$^+$-tipe Si, wat sterk met boron gedoteer is, en sy natuurlike oksiedlaag (SiO_2).

Vorige studies deur hierdie laboratorium het die lig-geïnduseerde ladingsoordrag-proses oor die natuurlik geoksideerde Si/SiO_2 tussenvlak bestudeer deur middel van THO, vir die geval van ongedoteerde Si. Daar is ook aanvanklike metings geneem met boron gedoteerde p$^+$-tipe Si/SiO_2 as monster.

Die THO sein vanaf natuurlik geoksideerde p$^+$-tipe Si/SiO_2 is in refleksie bestudeer. Die monster wat ondersoek is, is op 'n rekenaarbeheerde posisioneringstelsel geplaas wat die monster kon transleer en roteer. Die lasersisteem wat in die studie gebruik is, is in terme van sy spektrum, pulslengte, pulsfrekwensie, ruimtelike profiel en pulsenergie gekarakteriseer om te verseker dat kwantitatiewe metings uitgevoer kon word.

Defekte word by die Si/SiO_2 tussenvlak geskep deur die naby-infrarooi femtosekonde laserlig afkomstig van die laser wat gebruik is in die studie. Hierdie defekte word dan via multi-foton prosesse bevolk deur elektrone, en tot 'n mindere mate, gate. Hierdie ladingsoordrag oor die tussenvlak veroorsaak 'n elektrise veld oor die tussenvlak. Hierdie lig-geïnduseerde elektriese veld is bykomstig tot die ingeboude elektriese veld wat ontstaan as gevolg van ionisasie van die natuurlike tussenvlak-defekte deur die sterk dotering van die silikon met boron.

Dit is hierdie tussenvlak elektriese veld, bestaande uit die lig-geïnduseerde en die ingeboude elektriese veld, wat deur middel van THO ondersoek word. Die THO sein word sterk beïnvloed deur die sterkte van hierdie tussenvlak elektriese veld, aangesien die elektriese veld geïnduseerde tweede harmoniek opwekking (EVGTHO) sein alle ander bydraes tot die waargenome THO sein van Si/SiO_2 oorheers.

Die evolusie van die THO sein in tyd is genoteer vir verskillende intensiteite vanaf ongerepte sowel as vooraf bestraalde monsters. Hierdie data bied inligting oor die tydskale waarop die ladingskeiding plaasvind, sowel as wat die invloed van bestaande lig-geïnduseerde defekte op die ladingskeiding proses is. Die hoekafhanklikheid van die THO vir beide die aanvanklike sein (wanneer slegs die dotering geïnduseerde elektriese veld teenwoordig is) sowel as die versadigde sein (wanneer die elektron geïnduseerde veld domineer) is gemeet. Beide die metings vertoon 'n vier-voudige simmetrie maar met 'n

45° faseverskil tussen hulle. Hierdie faseverskil word as 'n bevestiging van die ommekeer in die elektriese veld rigting geneem. Die aanvanklike THO sein as 'n funksie van intensiteit is ook gemeet vir verskillende invallende golflengtes. Die afwyking van die nie-kwadratiese intensiteitafhanklikheid van die aanvanklike sein, word toegeskryf aan resonante twee-foton absorpsie en gepaardgaande afskerming van die tussenvlak elektriese veld deur ladingdraers.

Die metings wat uitgevoer is en die resultate wat verkry is dra by tot die verstaan van die lig-geïnduseerde ladingskeiding proses oor 'n tussenvlak van twee vastestowwe en spesifiek hoe dit van toepassing is by die belangrike Si/SiO_2 tussenvlak.

Acknowledgments

I would like to thank the following people and institutions:

- Prof. E.G. Rohwer, my supervisor and friend, for all the guidance, help and opportunities throughout my studies.

- All the members of the Laser Research Institute who provided an atmosphere within which it was a pleasure to do research.

- A special thanks to Gurthwin Bosman, who had to share a laboratory with me the last two years - not the easiest thing to do.

- Torsten Scheidt, for the foundation on which this study was based.

- Prof. H. Stafast, for all the advice and explanations that he offered when we had none.

- The National Research Foundation, Defence Peace Safety and Security (CSIR) and the Department of Labour, for funding my studies and the project.

- My parents for their unwavering support and encouragement.

- And last but in no means least, Marguerite Blignaut, who provided me with inspiration when I had none, motivated me when I was frustrated and supported me always.

This list is far from complete. To everyone who impacted positively on my studies throughout the years and all my friends who supported me, my sincere thanks and appreciation.

Contents

List of Figures

List of Tables

Introduction

Probably the most significant change in the world in the last century has been the influence that modern day electronic devices have had on our everyday lives. Modern society has become dependent on these devices and it would be hard to imagine the world without it. Micro-electronics has transformed the way we perceive and interact with our environment. It has transformed the way we think about global issues by allowing unparalleled access to information and computing power. Modern day electronic devices have become such an integral part of our day-to-day routine that they are hardly noticed and often taken for granted. Micro-electronics have infiltrated nearly every aspect of our lives with computers now regularly being found in everything from washing machines to automobiles. Supercomputers are working around the clock to try and find cures for terminal illnesses while the access to information made possible through the Internet and its supporting hardware have increased transparency in the affairs of governments and corporations. All these remarkable advances have been made possible by the simple silicon (Si) transistor.

As electronic devices became commonplace, industry has responded by creating ever faster, cheaper and more robust devices, pushing the very limits of physics in the quest for improved device performance. One of the key aspects in improving computing speed in a computer processor is the density of the transistors on a processor chip. As the density increases, not only does the total number of transistors and hence the total computing power increases, but the distances that signals have to travel decrease, leading to faster processor speeds. At these extreme densities employed today, the individual device dimensions shrink to microscopic levels. The most advanced processors now use transistor structures that are smaller than 45 nm across. This puts extremely stringent margins on the manufacturing parameters, as defects in such small devices play an ever increasingly important role. This is especially true when these devices are used in extreme conditions such as high temperature environments. One aspect of these ultra-small transistor devices that needs better understanding is the ultra-thin oxide layer that

covers the Si substrate. This oxide forms an insulating barrier between the Si and the metal contacts.

In order for device manufacturers to design and build these ultra-small transistor devices, they need an understanding of the influence of defects at this interface between the Si and this ultra-thin oxide layer. This interface region has properties that differ from those of the surrounding bulk Si and SiO_2. In order to understand the parameters of the design process, it is necessary to probe the properties of this interface, especially the electronic properties such as interfacial electric fields and charge trapping. By gaining insight into these properties, the design limits of devices can be better predicted. In order to probe these electronic properties, it is necessary to have a diagnostic tool that can access this buried Si/SiO_2 interface and which is sensitive to electric fields at this interface. One such optical technique, which is particularly suited to such a study, is second harmonic generation (SHG).

SHG has been around for quite a long time. It was first predicted in 1931 by Göppert-Mayer [1], nearly 30 years before the invention of the laser. As with most nonlinear optical effects, it was only after the invention of the laser that the effect was demonstrated. This was done by Franken *et al.* [2] in 1961, 30 years after the prediction by Göppert-Mayer. The field of nonlinear optics, especially SHG, grew immensely in this time as access to the high intensities achievable with lasers became more readily available. The power of SHG to analyze solid state materials and specifically buried solid-solid interfaces was soon realized, and in 1962, Bloembergen *et al.* [3, 4] developed a theoretical framework for describing SHG from surfaces and interfaces.

It is especially since the advent of affordable ultra-short and ultra-intense lasers the last 10 or so years that SHG from surfaces and interfaces have become an extremely active field of research, which has led to the investigation of various technologically important systems [5, 6]. The extremely high intensities and low average powers of these lasers enable the detection of SHG signals from interfaces and surface which otherwise would not have been possible. This has led to SHG becoming a very versatile tool for examining interfaces and surfaces.

As was mentioned earlier, the Si/SiO_2 interface is technologically extremely important as it is used in modern metal-oxides-semiconductor-field-effect-transistors (MOSFET's) which form the basis for modern micro-electronics. As evidence of its importance is the fact that it has been extensively studied for at least the last 30 years [7]. One of the methods of investigation has been SHG. Si/SiO_2 is an ideal candidate for SHG investigations, since it represents the boundary between a centrosymmetric crystalline solid (Si) and an amorphous solid (SiO_2). Since Si is centrosymmetric, SHG from the bulk is parity forbidden in the electric dipole approximation [8]. This symmetry

which inhibits SHG is however broken at the interface. This broken symmetry at the interface leads to a small but non-zero SHG susceptibility at the interface. This results in a unique interface sensitivity for SHG from centrosymmetric materials. This interfacial SHG signal was first experimentally observed by Brown *et al.* [9] in 1965. Since the symmetry is only broken at the interface, the SHG signal originates from only a couple of atomic layers at the interface.

Even though the Si/SiO_2 system has been so extensively studied, there are still a large number of unanswered fundamental questions. This is because there is currently no model describing the physical mechanisms responsible for the observed phenomena at this interface on a microscopic level [5, 10]. These phenomena include charge trapping, oxide leakage, defect creation, time dependent breakdown and hot electron effects. A number of these effects are related to the oxide growth process, and hence the understanding of these phenomena increases in importance as the oxide layer used in electronic devices thins (< 5 nm). A further effect which has not been sufficiently investigated in the past is the role that dopants in the Si play in the charge trapping at the interface. A high concentration of boron in the Si will ionize naturally occuring interfacial defects [11]. This results in a built-in electric field across the interface which can be probed by SH generation.

Most of the research regarding the Si/SiO_2 interface has focused on the technological aspects. However, the Si/SiO_2 interface is also interesting from a more fundamental point of view. As was mentioned earlier, it forms the boundary between a crystalline solid (Si) and an amorphous solid (SiO_2). This makes it a very interesting system in solid state physics as it allows for the study of the transition between these two phases. It is especially the optical properties, both linear and nonlinear, of the interface region (suboxide region) which is of interest, since this transition region varies considerably from those of the two adjacent bulk phases. SHG is an ideal tool to study this interfacial region since it can access this buried interface, is contactless and non-intrusive [12]. The Si/SiO_2 system has also been used as a test system for numerical calculations of the structural and optical properties of solid-solid interfaces [13].

In the next chapter, a brief summary will be given of the extensive research history regarding the Si/SiO_2 system. Special emphasis will be placed on the role that SHG has played and the success achieved with this method. A number of unresolved issues regarding the charge carrier dynamics, charge trapping as well as trap generation at the Si/SiO_2 will be highlighted. Mention will also be made of the little work that has been done with regard to the study of heavily doped Si, which defines the problem statement of this dissertation and puts it into perspective.

Chapter 1

Current state of research regarding the Si/SiO$_2$ system

Since the Si/SiO$_2$ interface is such an important system in modern day electronic devices, different techniques have been developed and employed to study the electrical and optical properties of the system, especially the influence of trap generation at the oxide interface. These techniques include, but are not limited to, electrical measurements [14], X-ray measurements [15], bombardment experiments [16, 17], electron spin resonance measurements [18, 19] as well as various types of electron microscopy such as ballistic electron emission microscopy (BEEM) [20], scanning electron microscopy (SEM) [21] and scanning tunneling microscopy [22].

Amongst the optical techniques, second harmonic (SH) generation has grown in importance because of its sensitivity to surfaces and buried interfaces, which gives it advantages over some of the techniques listed earlier. The non-invasive nature and atomic scale sensitivity along with the increasing availability and affordability of femtosecond lasers, makes SH investigations of interfaces a very active field of study. The most important work that has been done in this regard, particularly where it pertains to the Si/SiO$_2$ system, will be highlighted in the next paragraphs.

Most of the early work done on the Si/SiO$_2$ system was done with undoped Si. One of the earliest studies indicated that the SH signal originating from this interface showed a rotational anisotropy pattern that is determined by the structural symmetry of the surface, which is related to the crystalline face orientation, e.g. Si(100) or Si(111) [23, 24]. A number of researchers worked on a detailed theoretical description of the SH signal in reflection from centrosymmetric media and corresponding symmetry considerations. These include, but are not limited to, Sipe, Shen, Guyot-Sionnest, Lüpke, Bottomley, van Driel, Marowsky, Felderhof, Liebsch and their co-workers

[24, 25, 26, 27, 28, 29, 30, 31, 32, 33, 34, 35, 36, 37, 38, 39]. Lüpke produced an excellent review article, expanding on and summarizing the most important aspects regarding SH generation from centrosymmetric material in general and focusing on the Si/SiO$_2$ system [5].

Since SH generation can act as a non-invasive non-contact probe for the buried Si/SiO$_2$, it has been used extensively to monitor the oxidation process of Si surfaces [40, 41, 42]. In many cases the thickness of the oxide layer was monitored in this fashion, since the strength of the SH signal strongly depends on the oxide thickness [41]. It has also been determined that the P- and S-polarized SH response from the Si/SiO$_2$ shows different behaviour under P-polarized incident light. The S-polarized response from thick thermal oxide layers shows thickness dependent oscillations which can be attributed to multiple internal reflections in the oxide layer of the SH radiation [43]. The P-polarized thickness dependent response showed a strong deviation from this internal reflection model but can be described using quantum electrodynamics [44]. It is not only oxidation that is studied using SH generation. Other Si interfaces have also been studied using this technique where the Si surface was terminated with other chemical reactions [45, 46, 47]. One other Si-insulator interface that is gaining importance in the semiconductor industry, and has been examined through SH generation, is that of Si/SiO$_2$/Hf$_{(1-x)}$Si$_x$O$_2$ [48]. The reason for the interest is the high dielectric constants of HfO$_2$ and the Hf silicates.

It is possible to prepare the SiO$_2$ layer on the Si substrate using different techniques, for instance native oxidation, thermal oxidation, wet chemical processing, annealing and plasma oxidation. The preparation technique seems to influence the stoichiometry of the microscopic structure of the interfacial sub-oxide region (Si/SiO$_x$, $x < 2$). SH generation measurements can be used as a tool to probe this variation and can therefore be used as an indication of the preparation technique [49, 50, 51, 52, 53, 54, 55, 56, 57, 58]. SH generation has even been shown to be a sensitive probe for measuring interface roughness down to the Ångstrom level. Studies on samples where the interface roughness was systematically varied by preparing the samples under controlled conditions showed a sensitivity comparable to that of X-ray scattering [59, 60]. These SH measurements, when performed in conjunction with X-ray scattering and atomic force microscopy, can give an accurate measure of the interfacial roughness which is of great importance to device manufacturers that fabricate devices using these ultra-thin oxide layers.

Strong resonances within the SH spectra from Si/SiO$_2$ have been investigated using tunable laser sources [61]. These measurements have identified different types of resonances originating from a variety of electronic transitions that are specific to the interface. Two of these resonances (3.6 eV and

3.8 eV) can be ascribed to Si inter-band transitions at the Si(100)/SiO$_2$ interface. This transition is unique to the interface with no equivalent within the Si bulk [61]. Spectroscopic SH measurements can also be used to examine strain effects at the Si/SiO$_2$ interface and their subsequent influence on the interfacial bonding configurations. The main origins of the strain at the Si/SiO$_2$ interface are from the mismatch in the respective structures at the interface as well as the difference in thermal expansion coefficients between the Si and the SiO$_2$. This strain affects only a few monolayers of Si at the interface and results in a strong 3.3 eV resonance band from direct transitions between valence and conduction band states in these monolayers [62]. Strain is also responsible for redshifts of 40 meV and 70 meV in the inter-band critical points E_0' and E_1 from Si/SiO$_2$ when compared to those of the bulk Si [63].

As was mentioned earlier, a variation in the stoichiometry of the oxide layer can occur at the interface. This results in imperfect saturation of dangling bonds at the interface, which are described as interfacial defects. These defects play a key role in charge trapping which takes place at the interface. They also seem to exist mainly at edges. These edges, or atomic scale steps, that occur at the interface have been extensively investigated using rotational SH anisotropy measurements [64]. It is especially the defects at the vicinal Si(111)/SiO$_2$ interface that have been investigated [43, 49, 50, 51, 65, 66]. Different symmetry contributions (one- and three-fold respectively) in the rotational SH anisotropy can be attributed to steps and terraces at this interface [33, 43]. Specifically the off-cut angle with respect to the Si(111) surface seems to influence the rotational SH anisotropy pattern. This can be explained considering the orientation of the Si-O bonds located at the step edges [43]. Furthermore, the relative phases of the contributions from steps and terraces to the rotational SH anisotropy seem to change for oxides that have been prepared at annealing temperatures above 900 °C. These phase changes are attributed to alterations in atomic bonding configurations at the interfacial steps [49, 50, 51]. More recently, SH generation, in conjunction with reflectance-anisotropy spectroscopy, have been performed to monitor adsorption at Si(001) step-edges [67]. The motivation for the continuation of the research into the Si/SiO$_2$ system is that there is still no clear picture of the exact structure and the bonding configurations at the Si/SiO$_2$ interface. The importance of this knowledge for the manufacturing of MOS devices fuels this research [12, 68, 69, 70, 71, 72, 73].

Since this dissertation will focus on time dependent electric field induced second harmonic generation measurements of highly boron doped Si, the next paragraphs will elude to past measurements that have been performed regarding electric field induced second harmonic generation (EFISH) mea-

surements from the Si/SiO$_2$ system.

It has long been known that electric fields can influence the nonlinear optical properties of surfaces of centrosymmetric media [74]. The first measurements where this EFISH effect was examined at the Si/SiO$_2$ interface were performed by Aktsipetrov *et al.* [75]. In that study use was made of a MOS device where an external voltage was applied between the Si and the metal electrode attached to the SiO$_2$. This study showed the dependence of the strength of the generated SH signal as a function of the applied external voltage.

The first EFISH measurements of Si/SiO$_2$ without an externally applied voltage were performed by Mihaychuk *et al.* in 1995 [76]. The measurement showed a time dependent increase in SH intensity generated from a native Si/SiO$_2$ interface when irradiated by femtosecond laser pulses ($\lambda = 700$ nm, $\tau \sim 100$ fs). Since there was no external voltage applied, the increase in generated SH intensity could only be ascribed to a photo-induced effect. SiO$_2$ has a large band gap (8.9 eV) and is therefore transparent to the near infrared radiation. The increase in SH intensity could therefore not directly originate from the ultra-thin SiO$_2$ layer. Also, electronic effects within the bulk Si cannot account for the increase in SH intensity since the photo-induced carrier densities in the bulk Si are too low ($< 10^{18}$ cm^{-3}). The carrier recombination times in the bulk Si ($< 10^{-3}$ s) are also too short and do not correspond with the increase in SH intensity which occurs over a time scale of several minutes. It was tentatively suggested, and later widely accepted, that the increase in SH intensity is a result of an electric field that is optically induced across the Si/SiO$_2$ interface. It was proposed that electrons in the bulk Si were excited via a multi-photon process and transferred across the interface to the SiO$_2$. These hot electrons were subsequently trapped at the interface with the charge separation leading to an electric field across the interface. This interfacial electric field can attain values $> 10^4$ V/m which is sufficient to induce noticeable changes in the SH response of the interface. The temporal dependence of the SH intensity is a measure of the dynamics of the charge separation process. The EFISH intensity can also be used as a direct measure of the interfacial charge density [77].

Further studies by the same group found that the EFISH intensity caused by the electric field that is established due to photo-excitation of charge carriers is stronger for ultra-thin oxides and that oxygen can act as a catalyst for electron trapping at the SiO$_2$/air interface [78].

Another process that has been investigated with EFISH is gas adsorption and electron trapping on oxidized Si, with a universal mechanism, involving monopole (electron) - dipole (gas) coupling, proposed. This mechanism adequately explains the enhancement of the photo-induced electric field as

a result of ambient oxygen [79]. Oxygen is not solely responsible for charge trapping, as was shown with complementary SH generation and multi-photon photo-emission (MPPE) measurements on Si/SiO$_2$ samples that were exposed to oxygen in a chamber. These samples showed electron trapping in the SiO$_2$ even after the chamber was evacuated [77].

Recent studies, by a number of different groups, have employed EFISH measurements to study charge trapping at the Si/SiO$_2$ interface. The groups of Aktsipetrov, Downer, Kurz and Rasing [80, 81, 82, 83, 84, 85, 86, 87] studied MOS devices based on the Si/SiO$_2$ system, examining, amongst other things, the effect of the spatial charge distribution at the interface, the effect of oxide thickness on the EFISH signal, charge carrier screening effects and tunneled charge carriers being trapped near the Si/SiO$_2$ interface.

A group under Tolk used EFISH to measure the energy offsets between the Si and SiO$_2$ conduction bands [88]. They also used EFISH measurements to examine X-ray radiation damage in Si/SiO$_2$ [89]. Different types of trap sites at the Si/SiO$_2$ interface were studied by Fang *et al.* using EFISH measurements [90, 91] while photo-induced trap creation in Si/SiO$_2$ under near infrared femtosecond radiation was studied by Reider's group [92, 93]. Van Driel's group studied the effect of electron bombardment of Si/SiO$_2$ on surface charging and slow electron trapping in the ultra-thin SiO$_2$ by means of SH generation [94], while the group of Mitchell used an electrochemical cell with oxidized Si electrodes to show the effect of photo-generated charge carriers on the EFISH signal [95]. Fomenko *et al.* used SHG to investigate the active control of charge trapping in Si/SiO$_2$ by chemical modifications involving self assembled monolayers chemically bound to the SiO$_2$ surface [96].

The majority of EFISH studies on Si/SiO$_2$ have dealt with the effect of charge trapping of photo-induced electrons. Very few studies have considered the effect of photo-induced hole trapping at the interface, the most significant being those of Wang *et al.* [97, 98], Fomenko *et al.* [99] and Scheidt *et al.* [100].

Most of the research regarding EFISH has either dealt with photo-induced charge carriers contributing to the quasi-static electric field, or an externally applied bias voltage as origin of the electric field. The effect of heavy boron doping on the establishment of an interfacial electric field and therefore the EFISH signal was briefly investigated by Scheidt [11]. The study focused on the time dependent response of the doped p$^+$-type Si/SiO$_2$ system. The system showed an initial SH response associated with the doping induced electric field. This response was absent in the undoped samples. This initial signal decreased over a period of tens of seconds to a non-zero minimum, after which the signal increased over several minutes to an equilibrium value,

lower than that of the undoped Si. The study quantitatively examined the temporal behaviour of the SH signal but posed a number of questions to be answered.

It is the aim of this dissertation to expand on the work done by Scheidt and to further the understanding of the basic principles involved in photo-induced charge carrier transport and trapping in boron doped p^+-type Si/SiO₂. Apart from the fundamental nature of the study with respect to the physics of buried solid-solid interfaces and doping induced electrostatics, the ideas presented are relevant in the context of the technologically important field of device manufacture using ultra-thin oxides.

Chapter 2

Theoretical background

In the following chapter a brief description will be given of the relevant theory pertaining to this work. A systematic approach starting from Maxwell's equations incorporating the nonlinear polarization which leads to the nonlinear wave equation, will be followed. The theory surrounding the mechanisms of second harmonic (SH) generation, including the nonlinear susceptibility tensors, and how these result in a an anisotropic SH signal, as well as how external factors such as electric fields can influence the generated SH signal, will be discussed. This theory provides a basis for the experiments performed and the subsequent results, presented in the next two chapters.

2.1 Maxwell's equations

It is customary when discussing light-matter interactions to start with Maxwell's equations, written here in SI-units [101]:

$$\overrightarrow{\nabla} \cdot \vec{D} = \rho \tag{2.1}$$

$$\overrightarrow{\nabla} \cdot \vec{B} = 0 \tag{2.2}$$

$$\overrightarrow{\nabla} \times \vec{E} = -\frac{\partial}{\partial t} \vec{B} \tag{2.3}$$

$$\overrightarrow{\nabla} \times \vec{H} = \frac{\partial}{\partial t} \vec{D} + \vec{j} \tag{2.4}$$

where $\vec{D}$, the electric field inside a medium, is known as the dielectric field. It is related to the vacuum electric field, $\vec{E}$, through the following relation:

$$\vec{D} = \epsilon_0 \vec{E} + \vec{P} \tag{2.5}$$

where $\vec{P}$ is the response of the medium to the incident electric field, known as the polarization. In the case of dielectric media, which will be considered in this work, no free charges are present ($\rho = 0$) and no significant currents occur ($\vec{j} = 0$). All the media examined in this study are also non-magnetic ($\vec{B} = \mu_0 \vec{H}$). Under these conditions Maxwell's equations (Eqs. 2.1 - 2.4) can be summarized into the following wave equation:

$$\nabla^2 \vec{E} = \mu_0 \frac{\partial^2}{\partial t^2} \vec{D} \qquad (2.6)$$

Light matter interactions are usually considered within the framework of the Lorentz model [102], in which the electron is assumed to be bound in a harmonic potential to the nucleus. This is equivalent to expressing the response of the material, or rather the induced polarization of the material as a result of incident electromagnetic wave, as a linear function of the incident electric field:

$$\vec{P}(\vec{E}) = \epsilon_0 \chi^{(1)} \vec{E} \qquad (2.7)$$

where ϵ_0 is the permittivity of free space and $\chi^{(1)}$ is the first order optical susceptibility tensor which is a property of the material.

For large incident electric fields, as is the case when femtosecond laser pulses are incident on the medium and the electric field is of the same order as the inter-atomic binding force, the harmonic potential picture breaks down. This can be seen if one compares a harmonic potential to a real potential describing the binding forces on the electron. It can then be seen that the harmonic and real potentials only correspond for low energies (Fig. 2.1). It is therefore necessary to consider a more realistic potential when dealing with the interaction of femtosecond pulses with a medium.
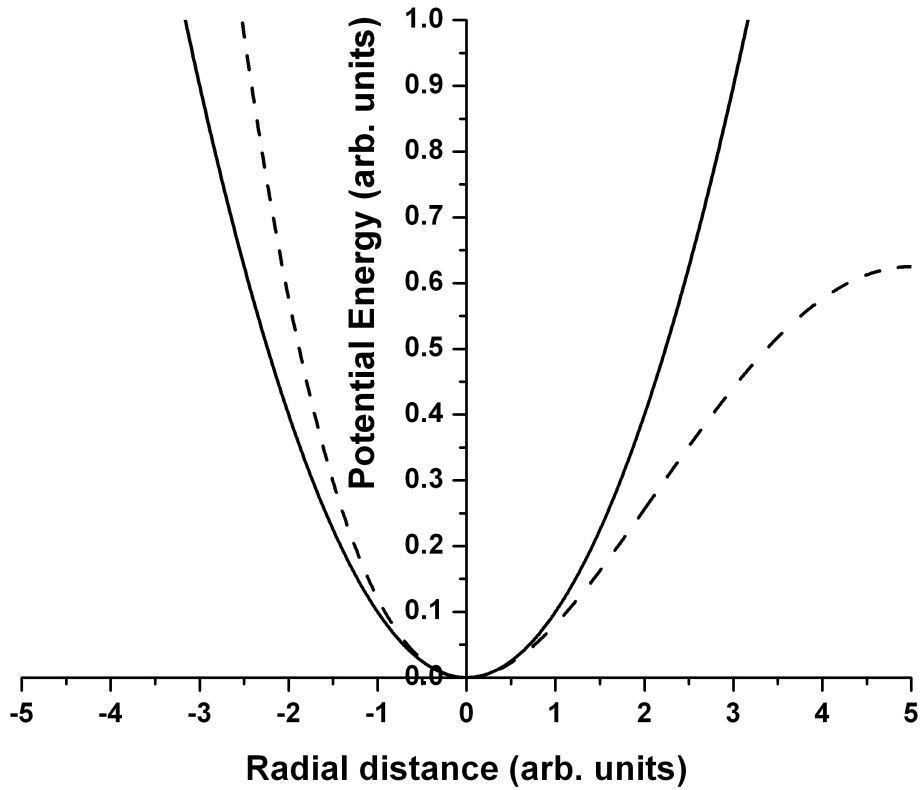
Figure 2.1: Diagram depicting a harmonic potential (solid line) and a generalized real potential (dashed line).

2.2　Nonlinear polarization and the nonlinear wave equation

The most general way of describing a realistic potential for an electron bound to an atom is to consider the potential as a power series in x, the displacement.

$$V(x) = \frac{1}{2}m\omega_0^2 x^2 + Ax^3 + Bx^4 + \dots \qquad (2.8)$$

This potential originates from the fact that any potential can be described by a Taylor series, which reduces to a power series if the physical shape of the potential is taken into consideration [102]. If one considers the electrons within a medium to be bound by such a potential instead of a harmonic one, the motion of the electron within the potential, driven by large electric fields,

is no longer harmonic. The polarization of the medium which depends on the displacement of the electrons within the incident electric field, is therefore no longer merely a linear function of the incident electric field.

Accepting Eq. 2.8 as the generalized potential, it is now possible to consider potential solutions for the response of the electron in such a potential, and hence the polarization of the medium. It can be shown that a solution for the polarization of the medium can merely be written as a power series of the incident electric field [102]

$$\vec{P}(\vec{E}) = \epsilon_0 \left(\chi^{(1)}\vec{E} + \chi^{(2)}\vec{E}\vec{E} + \chi^{(3)}\vec{E}\vec{E}\vec{E} + \dots \right) \tag{2.9}$$

where the $\chi^{(n)}$ are known as the n-th order optical susceptibility tensors. These tensors are material properties and determine how the incident electric field will interact with the material. The generalized polarization is usually rewritten as a sum of linear and non-linear terms:

$$\vec{P} = \vec{P}^{(1)} + \vec{P}^{NL} = \epsilon_0 \chi^{(1)}\vec{E} + \vec{P}^{NL} \tag{2.10}$$

Inserting Eq. 2.10 into the definition of the dielectric field (Eq. 2.5) leads to:

$$\vec{D} = \epsilon_0 \vec{E} + \epsilon_0 \chi^{(1)}\vec{E} + \vec{P}^{NL} = \epsilon_0 \left(1 + \chi^{(1)} \right)\vec{E} + \vec{P}^{NL} = \epsilon_0 \epsilon^{(1)}\vec{E} + \vec{P}^{NL} \tag{2.11}$$

with $\epsilon^{(1)} \equiv \left(1 + \chi^{(1)} \right)$, the first order dielectric tensor.

The dielectric field containing the nonlinear polarization can now be inserted into the wave equation (Eq. 2.6) to obtain the following result:

$$\nabla^2 \vec{E} - \frac{\epsilon^{(1)}}{c^2}\frac{\partial^2}{\partial t^2}\vec{E} = \frac{\partial^2}{\partial t^2}\mu_0 \vec{P}^{NL} \tag{2.12}$$

Eq. 2.12 represents the nonlinear wave equation, describing nonlinear optical effects in anisotropic, dispersive and lossless media. The nonlinear wave equation is a second order differential equation. To obtain a solution to this equation, it is necessary to consider the general case of dispersive media, where each frequency component of the field must be considered independently. It is thus necessary to describe the electric field vector, $\vec{E}(z,t)$, and the nonlinear polarization, $\vec{P}^{NL}$, as a sum over n positive frequency components, ω_n:

$$\vec{E}(z,t) = \sum_n E_n(z,t)e^{i(k_n z - \omega_n t)} + c.c. \tag{2.13}$$

$$\vec{P}^{NL}(z,t) = \sum_n P_n^{NL}(z,t)e^{i(k_n z - \omega_n t)} + c.c. \tag{2.14}$$

The propagation direction was chosen along the z-axis with k_n being the respective wave vectors. For optical frequencies, which are the only ones considered in this study, and pulse lengths in the order of 100 fs, the Slowly Varying Envelope Approximation (SVEA) applies [102]. Under the SVEA it is possible to linearize the nonlinear wave equation (Eq. 2.12) using the following approximations:

$$\frac{\partial^2}{\partial t^2} E_n \ll \omega_n \frac{\partial}{\partial t} E_n \qquad (2.15)$$

$$\frac{\partial^2}{\partial z^2} E_n \ll k_n \frac{\partial}{\partial z} E_n \qquad (2.16)$$

It can furthermore be assumed that for the nonlinear polarization where higher harmonics of the incident frequency act as carrier waves, the first order derivatives of the envelope functions can also be neglected:

$$\frac{\partial^2}{\partial t^2} P_n^{NL} \ll \omega_n \frac{\partial}{\partial t} P_n^{NL} \ll \omega_n^2 P_n^{NL} \qquad (2.17)$$

Inserting Eqs. 2.13 and 2.14 into the nonlinear wave equation (Eq. 2.12) and neglecting the relevant derivatives according to Eqs. 2.15 - 2.17, it can be seen that for each frequency component, ω_n, the following first order differential equation must be satisfied:

$$\left(\frac{\partial}{\partial z} + \frac{n_{\omega_n}}{c} \frac{\partial}{\partial t} \right) E_n(z,t) = i \frac{\omega_n}{2\epsilon_0 c n_{\omega_n}} P_n^{NL}(z,t) e^{-ik_n z} \qquad (2.18)$$

with n_{ω_n} being the refractive index for the specific frequency, ω_n. The general nonlinear wave equation (Eq. 2.12) has now been linearized (SVEA) and Eq. 2.18 now describes the electric field within a medium resulting from the nonlinear polarization.

2.2.1 Optical susceptibility tensors

As can be seen from Eq. 2.9 the polarization of a medium, exposed to electromagnetic radiation, is determined by the strength of the incident electric field and the optical susceptibility tensors. The optical susceptibility tensors, $\chi^{(n)}$, are material properties and are characteristic for the material. They are determined by the potential that describes the bonding of electrons in the specific medium. Since in the general case, the potential inside a medium is not isotropic in all directions, the optical susceptibility tensors need to reflect this anisotropy. These $\chi^{(n)}$-tensors are therefore tensors of rank $n+1$, which implies that, for example, $\chi^{(2)}$ has 27 elements and $\chi^{(3)}$ 81 elements. In general, the large number of elements within the optical susceptibility tensors

make them extremely difficult to determine exactly and therefore to predict the strength of nonlinear processes. Fortunately, this large number of elements can be reduced through physical considerations such as symmetry and certain approximations, most noticeably the Kleinman symmetry condition [103].

The intensity of the incident electric field on a medium determines which of the terms of the nonlinear polarization, P^{NL}, should be included in Eq. 2.18. In general, each subsequent higher order of optical susceptibility tensor is several orders of magnitude smaller than the previous one. The larger the incident electric field and subsequent intensity, the more relevant the higher order terms of Eq. 2.9 become. Each of the optical susceptibility tensors governs a specific type of nonlinear interaction. $\chi^{(2)}$ for instance, governs so-called 3-photon processes, which include sum- and difference frequency generation (of which second harmonic generation is a special case) and parametric amplification. $\chi^{(3)}$ governs 4-photon processes like four-wave mixing, self-focusing and self phase modulation.

2.3   Second harmonic generation

Second harmonic (SH) generation is a nonlinear process (governed by $\chi^{(2)}$) whereby light of frequency ω through interaction with a medium generates light of frequency 2ω. This process fulfills energy conservation requirements as two photons of frequency ω are required to produce one photon of frequency 2ω.

Since SHG is a $\chi^{(2)}$ process, it can be seen from Eq. 2.9 that the induced polarization at 2ω ($P^{(2\omega)}$) is proportional to the incident intensity ($I_\omega \propto E_\omega E_\omega$). In general it is not possible to measure electric fields oscillating at optical frequencies, and thus, in any experiment, it is the SH power which will be measured. The SH power is merely the spatial integral of the SH intensity ($I_{2\omega)}$) which will be proportional to the square of the incident intensity (I_ω)

$$I_{2\omega} \propto (I_\omega)^2 \tag{2.19}$$

Second harmonic (SH) generation is a well known technique for studying crystalline semiconductor material [5, 24, 104] and thin crystalline films. SH generation is particularly suited to this study since it is also able to probe buried interfaces (such as the Si/SiO_2 interface) and is sensitive to surface effects such as crystalline orientation, surface defects and surface roughness. The SH signal can also be influenced by electric fields that exist within the media and across the interface. This will be discussed further in Section 2.6.

SH generation has the advantage over other techniques that it is a non-contact, non-invasive measurement technique that is non-destructive. Different contributions to the second harmonic signal originate from the bulk and the interface of a material, since these regions have different effective second order susceptibilities. The measured SH signal is therefore a sum of both these contributions and it is generally impossible to separate these contributions in the measured signal.

2.4   SH rotational anisotropy

SH rotational anisotropy measurements are in general used to investigate the crystalline structure and crystalline orientation of materials. With this technique one is able to measure crystalline properties of thin films and interfaces and it is a complementary technique to X-ray diffraction measurements. The anisotropy in the SH signal under rotation of the sample around the incident beam, originates in the fact that the response of the medium (polarization) is not uniform in all directions within the medium. This implies that the orientation of the medium (crystal orientation) with respect to the incident light orientation (polarization of incident beam) can influence the strength of the generated SH response.

The optical susceptibility tensors are material properties that describe, amongst other things, the crystalline nature of the medium and hence the expected SH rotational anisotropy response. This implies that the crystal symmetry plays an important role in defining the values of the tensor elements. Since the tensor elements are determined by the crystal properties, the orientation of the crystal axis with respect to the incident electric field polarization determines the strength of the nonlinear polarization of the medium and hence the strength of the emitted SH wave.

Different crystal structures will therefore exhibit different SH anisotropy under rotation around the surface normal of the sample. These anisotropy patterns will also depend on the polarization of the incident electric field, P or S, and on the polarization that is observed, P or S, with P being the polarization which is parallel to the plane of incidence and S the polarization which perpendicular to the plane of incidence.

In general it is possible to measure four independent rotational anisotropy patterns for a specific medium, namely incident with P-polarization and detecting P-polarization, incident S-polarization and detecting P-polarization, incident P-polarization and detecting S-polarization and lastly incident S-polarization and detecting S-polarization. As an example of such measurements, Fig. 2.2 shows the four SH rotational anisotropy measurements per-

formed on a 5 μm thick sample of SiC on a Si substrate. This is the same sample used to measure the spot size at the focus of the experimental setup (Section 3.3). In the case of SiC, the SH signal originates from the SiC bulk.
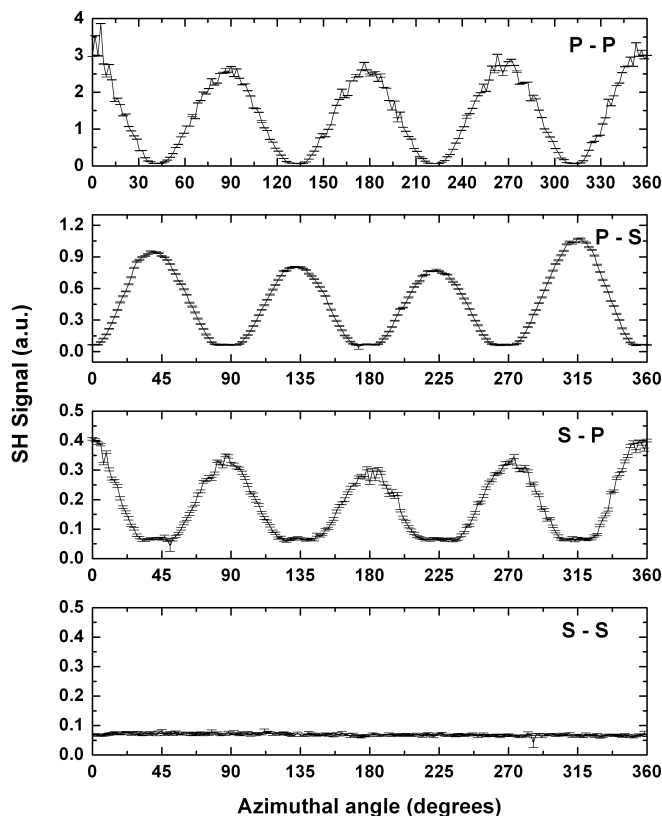
Figure 2.2: SH rotational anisotropy measurements from bulk SiC. The four polarization combinations employed were incident P and detection P (PP), incident P and detection S (PS), incident S and detection P (SP) and incident S and detection S (SS).

The SH rotational anisotropy measurements depicted in Fig. 2.2 allows for the determination of the specific polytype of SiC present in the sample. In this specific case the sample was 3C-SiC with (001) surface orientation. These measurements can be performed on a wide variety of media. As another example, rotational anisotropy measurements were also performed in this lab on bulk ZnO with wurtzite crystal structure [105]. As can be seen from Fig. 2.2 the P-P polarization combination has the strongest response. This is the case in general. This is also the reason why the P-P polarization combination was chosen for the all the measurements performed on p$^+$-type Si/SiO$_2$.

Since the symmetries of the bulk and surface are different, the anisotropy pattern from the two different sources can also be different. In this study, use is made of only P-polarized incident light and only P-polarized SH light is detected. The following expressions for the emitted P-polarized SH light, from both the bulk and surface contributions, can be obtained by performing the necessary transformations between the laboratory and crystal reference frames [33].

$$E_{P,P}^{surf,2\omega}(\phi) \propto \left[\sum_{n=0}^{3} a_{P,P}^n \cos(n\phi) \right] \cdot [E_P^\omega]^2 \qquad (2.20)$$

$$E_{P,P}^{bulk,2\omega}(\phi) \propto \left[b(P,P) + \sum_{n=0}^{4} c_{P,P}^n(\alpha,\beta) \cos(n\phi) \right] \cdot [E_P^\omega]^2 \qquad (2.21)$$

The Fourier coefficients $a_{P,P}^n$, $b(P,P)$ and $c_{P,P}^n(\alpha,\beta)$ are introduced here for the sake of simplicity and combine the relevant Fresnel factors, independent tensor elements and angular functions. Lüpke *et al.* compiled a more complete description including further algebraic detail, along with results for other polarization combinations [33].

The total generated SH intensity, originating from both the bulk and surface contributions, is proportional to the square of the absolute value of the sum of the respective contributing fields:

$$I_{P,P}^{2\omega} \propto \left| E_{P,P}^{surf,2\omega}(\phi) + E_{P,P}^{bulk,2\omega}(\phi) \right|^2 \qquad (2.22)$$

By combining Eqs. 2.20, 2.21 and 2.22, the total SH intensity generated from cubic centrosymmetric in reflection under P-polarized excitations, as a function of azimuthal angle, is obtained:

$$I_{P,P}^{2\omega} \propto \left| \sum_{n=0}^{4} c_n^{tot}(P,P) \cos(n\phi) \right|^2 \cdot (I_P^\omega)^2 \qquad (2.23)$$

with the Fourier coefficients $c_n^{tot}(P,P)$ combining the previous coefficients in Eqs. 2.20 and 2.21. It must be noted that Eq. 2.23 holds for crystal faces of $C_{1\mu}$ symmetry and is applicable to the low index cubic crystal faces (100), (111) and (110).

2.5 SH generation from centrosymmetric media

Centrosymmetric materials include a large number of media, for instance metals and elemental semiconductors such as Si. Considering the standard multipole expansion for fields, it can be shown that the electric dipole term is parity forbidden in the case of centrosymmetric materials [103]. This implies that SHG from the the bulk of such media is zero ($\chi_{bulk}^{(2)} = 0$) in the dipole approximation. The lowest order terms that can contribute to the nonlinear polarization of the bulk is the electric quadrupole and the magnetic dipole terms [106].

This symmetry, which ensures no SHG signal from the bulk of the material, is however broken at the surface or interface of the material and electric dipole effects are allowed ($\chi_{int}^{(2)} \neq 0$). The second order optical susceptibility responsible for SH at the surface or interface is however very small, giving typical yields of one SH photon for every 10^{13}- 10^{17} incident photons [5].

With extremely large electric fields and field gradients incident on the medium, as is the case when the medium is irradiated with femtosecond pulses, higher order (magnetic dipole and electric quadrupole) SH signals from the bulk and surface or interface of the material are induced which can be comparable in size, or even supersede, those from the symmetry breaking at the surface or interface [107].

One other contribution to the nonlinear polarization of centrosymmetric media is quasi-static electric field-induced dipole sources [106]. In fact, since SHG within the electric dipole approximation in centrosymmetric material is forbidden, SH generation from these materials is extremely sensitive to external perturbations, for example magnetic fields, quasi-static electric fields and strain [5].

This is exactly the case in Electric Field Induced Second Harmonic (EFISH) generation, where a quasi-static electric field that is present in the medium, perturbs the medium to such an extent that a large SH signal is observed. The resultant measured SH signal is the sum of the signals originating from all the different contributions, where the two most significant ones are the second order surface contribution and EFISH. The effective SH polarization can in this case be written as:

$$\vec{P}^{(2\omega)} = \epsilon_0 \left(\chi_0^{(2)} + \chi^{(3)} \vec{E}(t) \right) \vec{E}^{(\omega)} \vec{E}^{(\omega)} \tag{2.24}$$

where $\chi_0^{(2)}$ is the effective second order optical susceptibility originating from all other sources, $\chi^{(3)}$ is the third order susceptibility, $\vec{E}(t)$ is the quasi-static electric field in the sample and $\vec{E}^{(\omega)}$ is the incident electric field.

2.6 Electric Field Induced Second Harmonic

Electric fields in centrosymmetric media can perturb the structure of the media to such a degree that SH generation from the bulk of these media (or at least the region where the electric field is present) can be non-zero. In such cases the SH generation process is known as electric field induced second harmonic (EFISH) generation and the strength of the EFISH signal is an indirect measurement of the perturbing electric field strength.

The EFISH signal is governed by a $\chi^{(3)}$ process, as can be seen from Eq. 2.24. This would in general imply that the SH signal contribution from EFISH would be orders of magnitude smaller compared to the $\chi_0^{(2)}$ contribution which governs the SH signal from the interface. This is however not the case in Si/SiO_2. Since $\chi_0^{(2)}$ originates mainly from the interface, and hence from only a couple of atomic layers at the interface, it has a very small value. The electric field that can exist in the sample on the other hand, can obtain large enough values such that the EFISH signal completely dominates the interface contribution to the total SH signal.

Depending on the experimental conditions, EFISH can be the dominant contribution to the SH signal from Si/SiO_2. The electric field responsible for EFISH can have a number of different origins. Firstly, it can be externally applied. This is the case where MOS-devices (Metal Oxide Semiconductor) manufactured from Si/SiO_2 have been investigated and an external voltage was applied [83]. Secondly, the irradiation of the Si/SiO_2 interface by intense near infra-red radiation can induce an electric field across the interface via nonlinear electron and hole transport processes [100]. An important origin of an electric field across the Si/SiO_2 interface is heavy doping within the Si. The presence of a large number of boron atoms (p^+-doping) within the Si can ionize the existing defects on the interface and set up an electric field across the interface. This effect is investigated in detail in this dissertation.

It has been proposed [76, 78, 92, 100] that the following processes are responsible for the optically induced electric field that exists across the Si/SiO_2 under femtosecond irradiation. Firstly, defects are generated within the transparent ultra-thin (< 5 nm) oxide layer and on the interface. Electrons are then transported via a 3-photon process from the valence band of the Si into these generated trap-sites. The movement of these electrons and generation of the trap sites depends on the intensity of the radiation. The build-up of charge in these defects establishes an electric field across the interface.

It has also been shown that [100] at incident intensities > 45 GW/cm^2, hole trap sites are generated in the oxide layer and on the interface, and holes are transported via a 4-photon process from the Si into the generated trap sites. This movement of holes decreases the nett induced electric field.

The hole transport occurs on a much longer time scale to that of the electron transport, since it is a 4-photon process versus the 3-photon process of electron transfer. The transient SH signal is thus dependent on the nett interfacial electric field, $E(t)$, and the observed SH signal can be written as

$$I^{2\omega}(t) = \left| \chi_0^{(2)} + \chi_B^{(3)} E(t) \right|^2 (I^{\omega})^2 \tag{2.25}$$

where $\chi_B^{(3)}$ is the dipole allowed third order nonlinear susceptibility of Si and $\chi_0^{(2)}$ is the effective SH susceptibility arising from all other sources. $E(t)$ is the time-dependent nett interfacial electric field as a result of charge separation across the interface.

Since the EFISH contribution dominates the signal, the contribution from other sources can be ignored and thus the equilibrium SH signal is a direct measure for the interfacial charge density, n_c [77]

$$n_c \propto \left| \chi^{(3)} \vec{E}(t) \right| \propto \sqrt{I^{(2\omega)}} \tag{2.26}$$

2.7 The Si/SiO$_2$ system

Si is the most widely used semiconductor because it has a number of very useful characteristics. It is an abundant material, can be grown into large single crystals, can be both p- and n-doped and probably most important, it has a naturally occurring insulating oxide. This very thin (< 5 nm) oxide layer, along with the possibility of manufacturing p-n junctions, allows for the construction of complex devices such as transistors and MOS-structures.

Si has a diamond crystal structure and is hence centrosymmetric. This implies, as was stated earlier, that $\chi^{(2)}$ for the bulk is zero in the dipole approximation, and that any SH signal can only originate from the Si/SiO$_2$ interface or from a perturbation of the bulk, such as an electric field being present. Naturally occurring defects within the SiO$_2$ and on the interface of the Si/SiO$_2$ present trap sites for charges. Charges trapped in these sites influence the performance of devices constructed from the system. Understanding the formation of these trap sites and the dynamics of the charges being trapped, can lead to a better understanding of device performance.
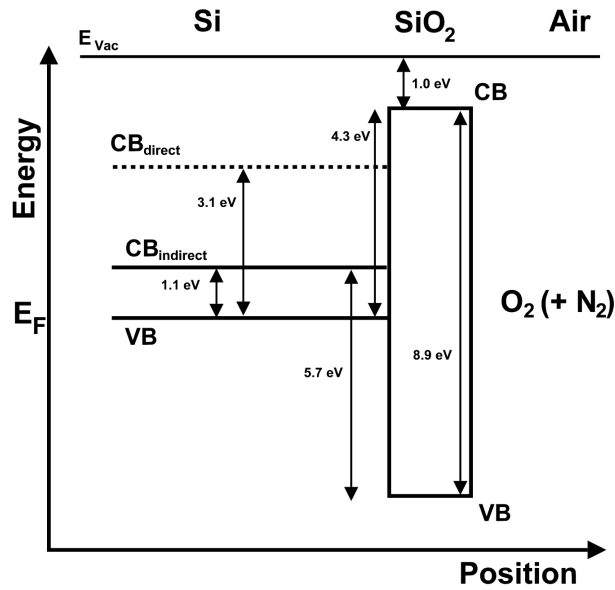
Figure 2.3: Simplified band structure of oxidized undoped Si.

As can be seen from Fig. 2.3 the energy barrier to transport electrons from the Si valence band (VB) into trap sites in the SiO$_2$ is 4.3 eV. This requires three NIR photons (assuming photons with energy 1.59 eV, $\lambda = 782.8$ nm) to surmount the barrier. In order to transport holes from the Si conduction band (CB$_{indirect}$) into trap sites in the SiO$_2$, four such photons are required to surmount the energy barrier of 5.7 eV. This implies that photo-induced charge carrier transfer across the Si/SiO$_2$ interface is a 3-photon process for electrons and a 4-photon process for holes. This then also explains the observed temporal SH response from undoped Si/SiO$_2$ depicted in Fig. 2.4.
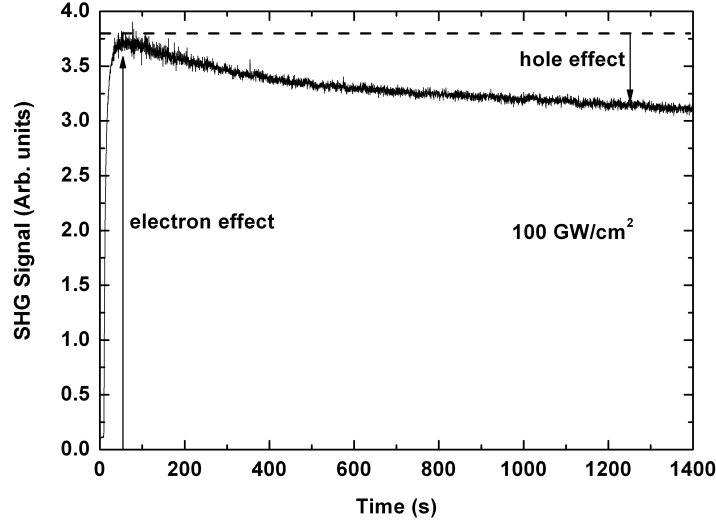
Figure 2.4: The temporal SH response from natively oxidized undoped Si/SiO$_2$ measured at an incident intensity of 100 GW/cm^2 showing the different effects due to electron transfer and hole transfer. The effects can be de-convoluted due to their different time scales.

The time dependent SH response shown in Fig. 2.4 can be reproduced by considering the trap formation processes (for holes and electrons) as two distinct processes and charge transfer processes (for holes and electrons) as a further two processes. Each of these processes is considered to be exponential and hence the following equation accurately reproduces the observed SH response in Fig. 2.4 [11, 76, 77, 100].

$$I^{(2\omega)} \propto \left(\sum_{i=1}^{4} a_i \exp(-t/\tau_i) \right)^2 \qquad (2.27)$$

Introducing dopants into the Si during manufacture, changes the fundamental characteristics of the system. By introducing boron, the Si becomes a p-type semiconductor. This implies that there is a depletion of electrons within the Si. If the doping is high enough, this effect can lead to the ionization of interface defect states which results in an electric field forming across the interface. This interfacial electric field contributes to the effective second harmonic susceptibility $(\chi_{eff}^{(2)})$ and hence the generated SH signal (EFISH). The purpose of this dissertation is the examination of this doping induced interfacial electric field on the EFISH signal.

Chapter 3

Experimental setup and methods

The following chapter describes the working of the commercial Ti:Sapphire femtosecond laser and the experimental setup used in this study. A femtosecond laser was chosen as it is possible to reach incident intensities in the order of 130 GW/cm^2 without significant heating of the sample. This is a direct result of the extremely short pulses ($\sim$ 80 fs) and low pulse energies ($\sim$ 10 nJ). As part of this work, the relevant laser parameters needed to be determined. This was done using a custom pulse characterization setup. Most importantly, the setup used for performing the SH measurements is also described. Lastly, this chapter deals with the preparation and properties of the highly boron doped p$^+$-type Si/SiO$_2$ samples studied in this work.

3.1 Laser system

The most common laser material employed to generate ultra short femtosecond pulses is titanium doped sapphire (Ti:Sapphire). This is because of the strongly broadened fluorescence band due to lattice vibrations (phonons). This results in a laser gain line shape, in lasers using Ti:Sapphire as active medium, that covers the spectral range of 660 - 1180 nm with a maximum at 795 nm [108]. The shortest temporal pulse duration obtainable is related to the spectral pulse width through the Fourier theorem, where the temporal pulse width is inversely proportional to the spectral bandwidth. This implies that the theoretical temporal pulse limit attainable from Ti:Sapphire is 4 fs. The shortest pulse length ever achieved directly from an oscillator is 5.4 fs [109] while a pulse length close to the theoretical limit has been achieved by means of external pulse compression [110].

Ultra short pulses are formed when many longitudinal modes (present in Ti:Sapphire lasers as a result of the broad fluorescence spectrum) with

a fixed phase relation interfere constructively. In a Ti:Sapphire laser this is achieved through Kerr-lens-modelocking [111]. The third order susceptibility of Ti:Sapphire results in a refractive index which is intensity dependent, $n(I) = n_1 + n_2 I$, with $n_2 = 3.1 \times 10^{-16} \text{cm}^2/\text{W}$. This implies that intense laser modes that have a transverse intensity distribution experience a transverse refractive index profile within the gain crystal. This results in focusing of the intense laser mode (selffocussing). Longitudinal modes within the cavity that randomly interfere constructively are more intense than cw modes and therefore undergo stronger selffocussing within the Ti:Sapphire crystal. The oscillator cavity is designed such that it has a higher quality, i.e. lower losses for these focused modes. The intense, focused modes are amplified while the cw modes die out. This can easily be done by introducing a aperture or slit into the cavity. This effect is known as Self Amplitude Modulation (SAM).

The longitudinal intensity distribution of the short intense pulse introduces an intensity dependent phase shift know as Self Phase Modulation (SPM). For $n_2 > 0$, as is the case with Ti:Sapphire, this introduces positive temporal pulse spread, also known as frequency chirp. This implies that the blue components of the pulse spectrum are delayed compared to the red components, leading to temporal broadening. Positive temporal spreading is also introduced by the optical components within the laser cavity such as mirrors and lenses. This effect is also referred to as positive group velocity dispersion (positive GVD). In order for the laser to attain stable modelocking and to achieve the shortest possible pulses, it is necessary to compensate for this positive GVD. This is done by inserting into the cavity two pairs of prisms. Prisms introduce anomalous or negative GVD. In this fashion it is possible to exactly compensate for the positive GVD and obtain the shortest possible pulses and stable modelocked operation.
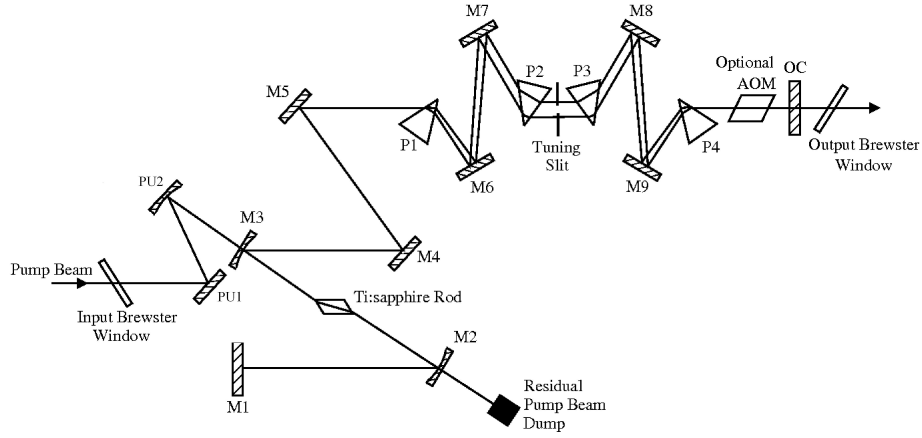
Figure 3.1: Layout of commercial (Spectra Physics, Tsunami) femtosecond oscillator.

Figure 3.1 shows the layout of the laser system used in this study. It is a commercial femtosecond oscillator (Spectra Physics, Mountain View, CA, USA, Tsunami). The oscillator is pumped by an intra-cavity frequency doubled Nd:YVO$_4$ laser (Spectra Physics, Millenia V) which produces a maximum cw power of 5.5 W at a wavelength of 532 nm. The pump beam enters the laser cavity through a Brewster window and is directed and focused into the Ti:Sapphire crystal by mirrors PU1 and PU2. M2 and M3 are highly transmissive for the pump wavelength (532 nm) but highly reflective for the near infrared (NIR) laser wavelength. These two mirrors form part of the laser cavity. The residual pump beam which is not absorbed in the crystal is dumped onto a beam block behind M2. M1 forms the one end mirror of the cavity. P1 - P4 are the pairs of prisms inserted into the cavity to introduce negative GVD to compensate for the inherent positive GVD of the system. P2 and P3 can be moved up and down, introducing more or less negative GVD depending in their positions. In this fashion the pulse length can be optimized. A tuning slit of constant width but adjustable position is introduced between P2 and P3, allowing for wavelength tuning. The beam exits the cavity through the output coupler (OC) and passes through a Brewster window before leaving the laser. An optional acousto-optical modulator (AOM) is also introduced into the cavity to assist with initiating modelocking and to help maintain stable operation.

3.2 Laser characterization

In order to perform quantitative SHG experiments it is necessary to characterize the relevant properties and parameters of the laser system used in the experiments. The pulse repetition rate of the laser was measured with a custom built pulse train detector. The pulse spectrum was measured with a charged coupled device (CCD) array spectrometer (Ocean Optics, Dunedin, FL, USA, HR4000 VIS-NIR). The average power of the laser was measured with a commercial power meter (Coherent, Santa Clara, CA, USA, Fieldmaster with LM-3 measurement head). A custom built autocorrelator (Fig. 3.2), based on a Michelson interferometer, was used to measure the temporal pulse width.
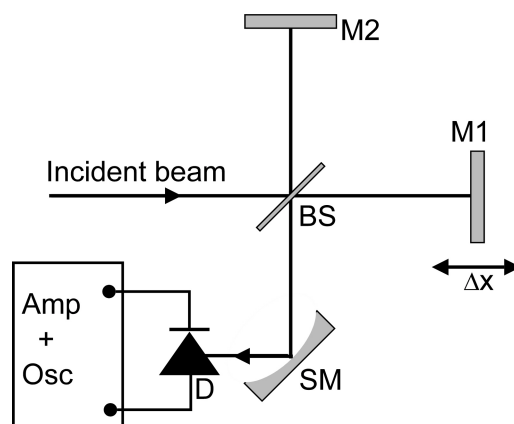
Figure 3.2: Layout of the autocorrelator used for measuring the pulse. M1: mirror on movable speaker, M2: static mirror, BS: beam splitter, SM: spherical mirror, D: AlGaAs detector diode, Amp: amplifier, Osc: oscilloscope, Δx: optical path length difference.

The laser pulse duration needed to be measured to be able to determine the intensity incident on the sample during the experiment. In order to measure the pulse duration, the laser pulses to be measured are split by a 50/50 beam splitter (BS) into two pulses, P1 and P2. These two pulses are reflected back onto themselves by mirrors M1 and M2. M2 is placed on a standard audio speaker. By driving the speaker by a low frequency signal generator, a variable delay on P2 is introduced. Finally P1 and P2 (with P2 having a variable temporal delay introduced) are focused by a spherical

mirror onto a reverse biased AlGaAs light emitting diode (LED) (Kingbright Elec. Co. Ltd., Taipei, Taiwan, L-1513SRC-E) used as a detector diode.

The AlGaAs detector diode has a band gap of $\sim$1.9 eV. This is considerably higher than the photon energy (1.59 eV) of the laser pulses at a center wavelength of 782.8 nm. This results in single photon absorption being suppressed in the diode and two photon absorption dominating. The resultant photo-current (PC) is an interference pattern (commonly referred to as the interference autocorrelation trace) which is a function of the temporal delay between P1 and P2, Δt. The temporal delay, Δt, is determined by the spatial delay introduced by the speaker, Δx ($\Delta t = \Delta x / c$).

With the autocorrelator properly aligned, the ratio between the peak photo-current, PC_P, (signal when the two pulses are perfectly overlapped) and the background, PC_{BG}, (when the two pulses do not overlap at all) should be 8:1. This ratio is obtained because of the two-photon absorption process in the diode.The ratio of the respective signals can be determined as follows:

$$\frac{PC_P}{PC_{BG}} \propto \frac{I_P^2}{I_{BG}^2} \propto \frac{\left(|E_{P1} + E_{P2}|^2\right)^2}{\left(|E_{P1}|^2\right)^2 + \left(|E_{P2}|^2\right)^2} = \frac{(2 \cdot E_{P1})^4}{2 \cdot (E_{P1})^4} = \frac{16 \, (E_{P1})^4}{2 \, (E_{P1})^4} = \frac{8}{1}$$

(3.1)

This is because $E_{P1} = E_{P2}$ since each pulse is split into two parts of equal intensity by the 50/50 beam splitter.
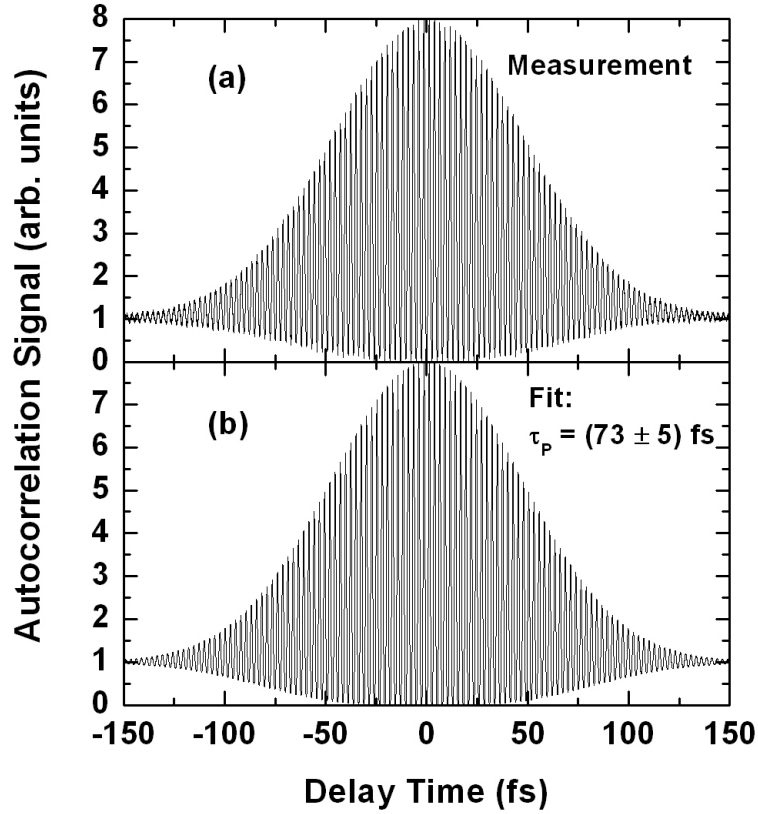
Figure 3.3: Typical second order interference autocorrelator measurement (a) and fit to the data (b) with pulse length, τ_P, and induced phase shift, ϕ, as fit parameters, of the femtosecond pulses employed in this study. The extracted pulse length was (73 ± 5) fs.

Fig. 3.3(a) shows a typical autocorrelation trace of the laser pulses used in this study. From this trace it is possible to extract the pulse length. Fig. 3.3(b) is the fit to the data used to extract the relevant parameters like the pulse length. The autocorrelation measurement agrees with the predicted 8:1 ratio between the peak signal and the background. The fit assumes a Gaussian temporal envelope and a sinusoidal carrier wave for the measured pulse.

The electric fields of P1 and P2 can be described as:

$$E_{P1}(t) = E_{P1} \cdot e^{-2t^2/\tau^2} \cdot \sin(\omega t) \tag{3.2}$$

$$E_{P2}(t) = E_{P2} \cdot e^{-2(t-\Delta t)^2/\tau^2} \cdot \sin(\omega(t - \Delta t) + \phi) \tag{3.3}$$

In these two equations, ω is the frequency of the carrier wave, and the $1/e$ width of the electric field envelope is $\sqrt{2} \cdot \tau$. The phase shift between the two pulses introduced by the beam splitter is ϕ and Δt is the temporal delay between the two pulses. Since the photo-current signal produced in the detector diode is as a result of two-photon absorption, the photo-current signal ($PC(\Delta t)$) will be proportional to the square of the total intensity ($PC(\Delta t) \propto I^2$) incident on the detector, integrated over time, t.

$$PC(\Delta t) \propto I^2(\Delta t) = \int \left(|E_{P1}(t) + E_{P2}(t - \Delta t)|^2 \right)^2 dt \tag{3.4}$$

Eq. 3.4 represents a convolution integral, which fully describes the observed autocorrelator trace (Fig. 3.3) in terms of the measured electric fields. This equation can be used to extract the relevant pulse parameters. The spectral frequency, ω, is measured directly (see below) while the electric field envelopes (E_{P1} and E_{P2}), the induced phase shift (ϕ) and temporal pulse width (τ) are extracted from a fit of Eq. 3.4 to the experimental measurement.

The temporal pulse width of a laser pulse is usually described in terms of the full width at half maximum (FWHM) of the intensity envelope. Since the intensity is proportional to the square of the electric field ($I \propto E^2$), the temporal pulse width of the intensity envelope (FWHM), τ_P, is related to the electric field pulse width, τ, through:

$$\tau_P = \sqrt{\ln 2} \cdot \tau \tag{3.5}$$

The extracted pulse width for the measurement shown in Fig. 3.3(a) was $\tau_P = 73 \pm 5$ fs.
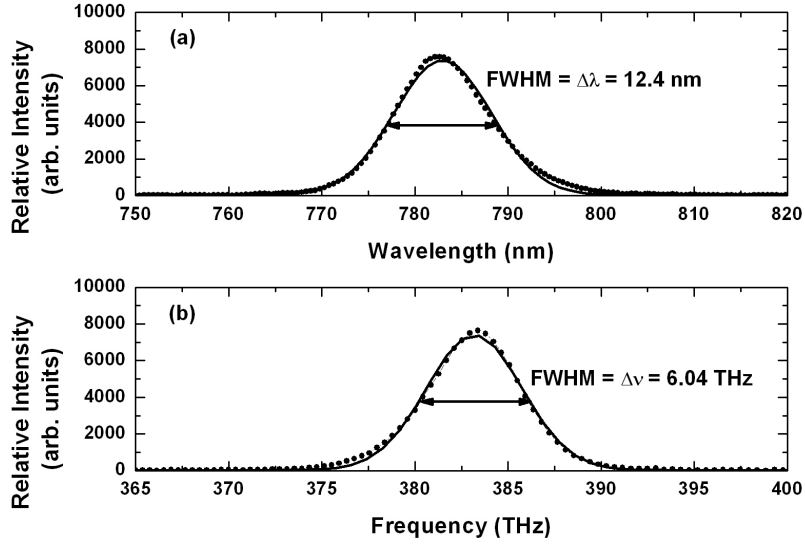
Figure 3.4: Spectrum from Ti:Sapphire laser in wavelength (a) and frequency (b). A Gaussian fit, used to extract the bandwidth, is also shown (solid lines) for both graphs.

As was mentioned earlier, the spectral composition was measured using a CCD array spectrometer. Fig. 3.4(a) shows a typical spectral measurement. Fig 3.4(b) shows the same measurement, but in the frequency domain. The spectral pulse width in terms of wavelength and frequency was extracted by performing a Gaussian fit to the data for the measured pulse and was found to be 12.4 nm and 6.04 THz respectively. As was mentioned earlier, the spectral width and temporal width are related through the Fourier theorem. The time-bandwidth-product (TBP) $\tau_P \cdot \Delta\nu$ for the measured pulse was determined to be 0.44 ± 0.04 which compares well to the theoretical limit for a Gaussian pulse which is 0.44. It can therefor be assumed that the pulses are bandwidth limited.

The pulse repetition rate was measured with a simple custom built pulse train detector. The measurement can be seen in Fig. 3.5 and the repetition rate was found to be 80 MHz.
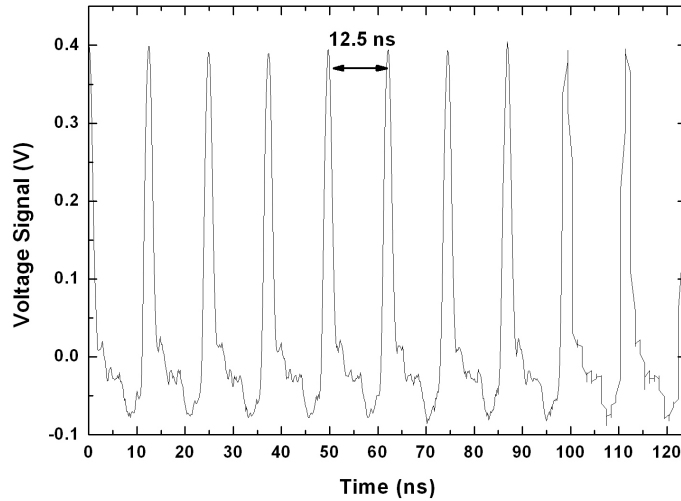
Figure 3.5: Pulse train from Ti:Sapphire laser. The period was measured as 12.5 ns which corresponds to a pulse repetition rate of 80 MHz.

The spatial distribution of the pulse energy needs to be measured in order to calculate the intensity incident on the sample. The spatial distribution of the pulse was measured with a CCD camera (Spiricon, Logan, USA, SP980M) (Fig. 3.6) and was found to be close to Gaussian TEM_{00}. Since the beam is approximately Gaussian, it can be assumed that the beam would maintain this Gaussian profile in the tightly focused spot on the sample during the experiment. This allows for the calculation of the intensity incident on the sample.
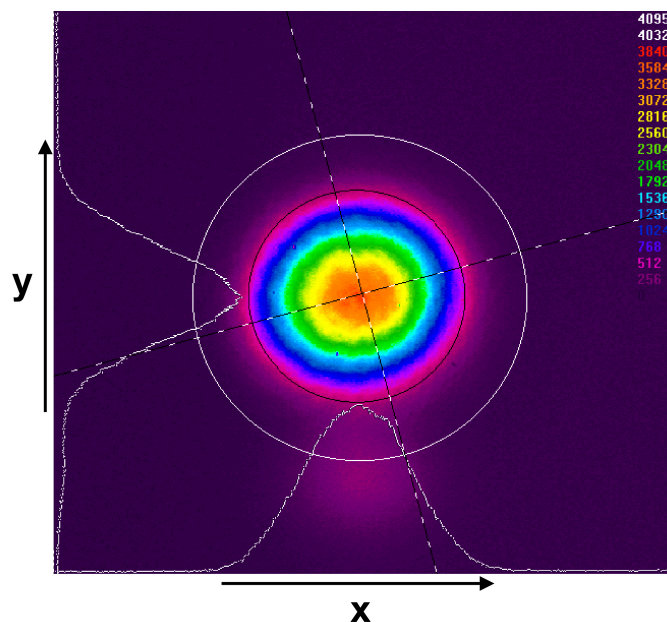
Figure 3.6: CCD camera picture of transverse beam shape. The beam profile is $\approx \text{TEM}_{00}$.

The average laser power, monitored over a period of 3 hours, did not vary by more than 3%. The output of the laser was vertically polarized. The pulse peak power is determined by assuming a Gaussian temporal intensity envelope and was hence calculated to be $P_{max} = 0.94 E_P / \tau_P$ where E_P is the maximum total pulse energy. The important laser parameters are summarized in Table 3.1. These values are applicable to the laser pulses as they are incident on the sample being investigated.

Table 3.1: Important parameters of the Ti:Sapphire laser used in this study.

Max average power	P_{av}	840 mW
Repetition rate	f_{rep}	80 MHz
Max pulse energy	E_P	10.5 nJ
Min pulse duration	τ_P	(73±5) fs
Max pulse power	P_{max}	135 kW
Center wavelength	λ	782.8 nm
Spectral width	$\Delta\lambda$	(12.4±0.5) nm
Time-bandwidth-product	$\tau_P \cdot \Delta\nu$	0.44±0.04 ($\approx$ theoretical limit)
Max pump power	P_{Pump}	5.5 W
Pump wavelength	λ_{Pump}	532 nm
Radial mode		$\approx$ TEM$_{00}$
Polarization		vertical

3.3 Experimental layout

The layout of the experimental setup used to perform the SH experiments is shown in Fig. 3.7. The fundamental beam is guided by two gold coated mirrors, both labeled M1, (Edmund Ind. Optics, Barrington, NJ, USA, protective coating, 1/4 wave surface accuracy at 632.8 nm) through first a $\lambda/2$-retarder plate (B. Halle Nachfl. GmbH, Berlin, Germany) and then a polarizer P1 (Halbo Optics, Chelmsford, UK). This combination allows for the continuous attenuation of the pulse energy by rotating the $\lambda/2$ plate, and selecting the desired incident beam polarization by rotating the polarizer P1. The beam then passes through a long-pass filter F1 (Edmund Ind. Optics, transmission $<$ 1% ($>$ 90%) for wavelengths $<$ 570 nm ($>$ 620 nm)) to eliminate any SH light that might have been generated by the beam passing through the optical components from reaching the sample or the detector. The fundamental beam is then focused onto the sample by an achromat lens L1 (Edmund Ind. Optics, focal length f = 35 mm, NIR anti reflection (AR) coated).
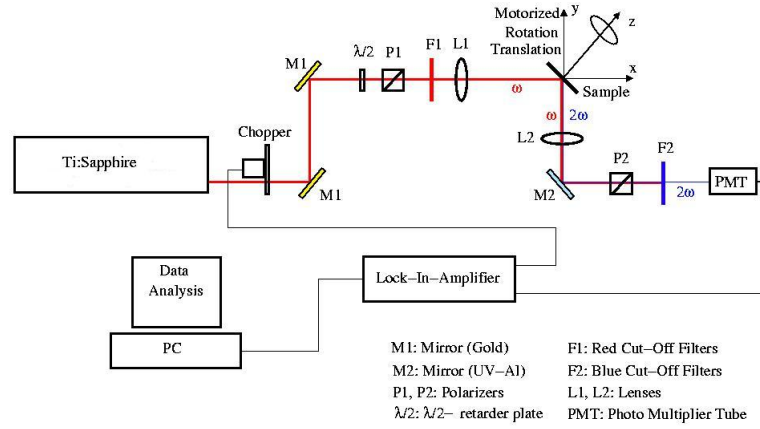
Figure 3.7: Diagram of the experimental setup employed to perform the SH measurements. Ch: Light chopper. M1: Gold coated mirrors. $\lambda/2$: Retarder plate. P1, P2: Polarizers. F1: Red cut-off filter. L1, L2: Lenses. M2: UV - Al coated mirror. F2: Filter set. PMT: Photomultiplier tube. A lock-in-amplifier and automated data acquisition was employed.

The angle of incidence of the beam on the sample was kept constant at 45° during all the experiments. The SH experiments were all performed in reflection. The reflected light from the sample was collimated using a double convex lens L2 (Edmund Ind. Optics, f = 125 mm, VIS-NIR AR coated) before being steered by an aluminium mirror (Edmund, Ind. Optics, UV enhanced aluminium coating, 1/4 wave surface accuracy at 632.8 nm) through an analyzer P2 (Halbo Optics). The generated SH signal is then separated from the fundamental frequency by a combination filter set F2 consisting of a short-pass filter (Edmund Ind. Optics, transmission < 1% (> 95%) for wavelengths > 525 nm (< 490 nm)) and a narrow band band-pass interference filter (Thin Film Products, Cambridge, MA, USA) with a transmission band of 10 nm centered at 391.4 nm. For the experiments performed at wavelengths other than an incident wavelength of 782.8 nm, the band-pass filter was replaced with a short-pass filter (Schott AG, Mainz, Germany, BG-39, transmission > 60% (< 0.01%) for wavelengths between 350 nm and 590 nm (> 700 nm).

The SH signal was detected by a sensitive photomultiplier tube (PMT) (Hamamatsu Photonics K.K., Japan, H6780-03). The small signal from the PMT was first amplified with a fast amplifier (Hamamatsu Photonics K.K., C5594) before being amplified in a quasi cw fashion, averaging over the 80 MHz signal, by a lock-in-amplifier (Ithaco Inc. NY, USA, Dynatrac Model

393), used in combination with a 500 Hz light chopper, Ch (Ithaco Inc, Model 383A). For the rotational anisotropy measurements described in Section 3.4.3, the lock-in-amplifier and light chopper was replaced by a boxcar integrator (Stanford Research Systems, SR250) to improve the signal to noise ratio. This left the temporal resolution (of 0.2 s) unchanged as the boxcar allowed for the averaging over many pulses.

The data acquisition was automated using commercial software (National Instruments, Austin, TX, USA, LabView) and an analog-to-digital (A/D) converter (Eagle Technology, Cape Town, South Africa, ISA PC-30F). The sampling rate was 700 Hz and data point averaging was employed.

The sample is mounted on a 3D automated translation stage (Newport, Irvine, CA, USA) which enables the recording of SH signal as a function of X- and Y-position as well as azimuthal angle of rotation about the Z-axis. The maximum experimental resolution is 0.9° rotational angle and 5 μm spatial resolution. The data acquisition allows for a 0.2 s temporal resolution.

The setup also allows for the recording of the SH signal dependent on the polarization of the incident fundamental and the analyzed SH. Four combinations are possible, with the fundamental wave being either P- or S-polarized as well as the analyzed SH signal being analyzed in either the P- or S-polarization direction. These four possibilities are denoted P-P, P-S, S-P and S-S. All the measurements performed in this study were done with a P-P combination.

The wavelength of the fundamental was 782.8 nm for the rotational anisotropy measurements and interrupted time-dependent measurements but was varied for the charge carrier screening effect measurements.

Since it is difficult to measure the intensity of the laser fundamental at the sample surface, use is made of the z-scan technique to determine the Rayleigh length and hence the spot size at the focus. This entails measuring the generated SH power $P_{2\omega}(z)$ as a function of the sample position along the beam propagation direction (z-axis). It is possible to correlate the measured SH power to the focal spot size by making use of standard Gaussian beam propagation theory [102]. A sample (5 μm thick SiC on Si substrate) that shows no time-dependent SH response under femtosecond irradiation was used for this measurement. In this fashion the intensity at the focus can be determined.

For this analysis, it is necessary to assume an elliptical Gaussian function for the transverse spatial intensity profile of the fundamental wave, since the fundamental wave is incident at an angle of $\theta = 45°$ on the sample:

$$I_\omega(x,y) = I_{\omega_0} \cdot \exp(-2x^2/w^2) \cdot \exp(-2\cos^2\theta \cdot y^2/w^2) \qquad (3.6)$$

I_{ω_0} denotes the intensity of the fundamental beam in the center of the beam ($x = 0$, $y = 0$) with $w = w(z)$ the radius of the fundamental beam at position z along the propagation direction. According to the assumed Gaussian intensity envelope for the fundamental, $w(z)$ denotes the $1/e$-beam radius of the electric field envelope. The beam radius $w(z)$ is also related to the Rayleigh length z_R through [102]

$$w = w(z) = w_0 \cdot \left(1 + z^2/z_R^2\right)^{\frac{1}{2}} \tag{3.7}$$

with

$$z_R = \pi w_0^2 / \lambda \tag{3.8}$$

and $\lambda = 2\pi c/\omega$. $w_0 = w(z)$ denotes the minimum beam radius at $z = 0$.

The power of the incident fundamental as a function of the sample position z can be calculated by evaluating the following integral: $P_\omega(z) = \int \int I_\omega(x, y, z) dx dy$ yielding

$$P_\omega(z) = I_{\omega_0} \frac{\pi w(z)^2}{2\cos\theta} \tag{3.9}$$

Considering Eq. 2.19, which shows that the measured SH intensity is proportional to the square of the incident intensity, the following expression describes the transverse spatial intensity distribution

$$I_{2\omega} = \gamma \cdot I_\omega^2(x, y) = \gamma I_{\omega_0}^2 \cdot \exp(-4x^2/w^2) \cdot \exp(-4\cos^2\theta \cdot y^2/w^2) \tag{3.10}$$

assuming that Eq. 3.6 describes the intensity distribution of the fundamental. Here γ has been introduced as the SH conversion efficiency coefficient. In order to obtain the SH power it is necessary to spatially integrate over the SH intensity. This yields

$$P_{2\omega} = \gamma \cdot I_{\omega_0}^2 \cdot \frac{\pi w^2}{4\cos\theta} \tag{3.11}$$

By comparing Eq. 3.9 and Eq. 3.11 it can be seen that

$$P_{2\omega} = \gamma \cdot P_\omega^2 \cdot \frac{\cos\theta}{\pi w^2} = \frac{K}{w^2} \tag{3.12}$$

with $K = \gamma \cdot P_\omega^2 \cdot \frac{\cos\theta}{\pi}$. By inserting Eq. 3.7 into Eq. 3.12, an equation describing the SH power as a function of z-position is obtained:

$$P_{2\omega} = P_{2\omega}(z) = \frac{K}{1 + z^2/z_R^2} \tag{3.13}$$

Eq. 3.13 can now be fitted to a measurement of the SH power as a function of z-position, with K and z_R as fit parameters. Figure 3.3 shows a typical measurement with the solid curve being a fit according to Eq. 3.13. From this fit the Rayleigh length was extracted and found to be 0.19 mm. This corresponds to a beam waist, according to Eq. 3.8, of $w_0 = 6.9$ μm. The spot diameter therefore corresponds to 13.8 μm. In all the experiments performed here, the sample was placed at $z = 0$.
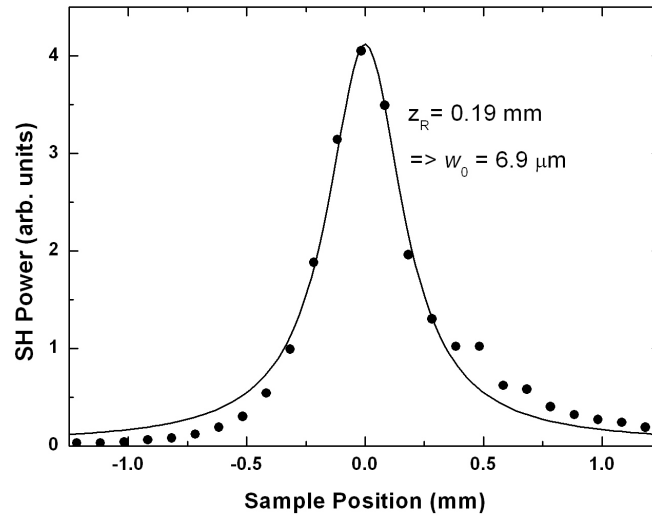
Figure 3.8: Measurement of the beam radius at the sample position. The solid line is a fit according to Eq. 3.13 which was used to extract the Rayleigh length, $z_R = 0.19$ mm, which corresponds to a beam waist (radius) of $w_0 = 6.9$ μm.

Using Eq. 3.9, and the value for the maximum pulse power $P_{max} = 130$ kW listed in Table 3.1, the maximum possible peak intensity incident on the sample is determined as ≈ 125 GW/cm^2, although this extreme intensity is never employed in this work.

3.4 Types of SH experiments

This study deals with four types of SH measurements. These measurements are time dependent SH measurements of virgin samples, SH measurements of pre-irradiated samples, rotational anisotropy SH measurements and the

measurement of charge carrier screening through resonantly enhanced two-photon absorption of highly boron doped p$^+$-type Si/SiO$_2$.

3.4.1 Time dependent SH measurements

A study of the SH response from Si/SiO$_2$ is a study of the EFISH signal, and hence the electric field across this interface. The effect of the doping induced initial interfacial electric field as well as the effect of photo-induced charge transfer across the interface can be monitored by measuring the SH response from the sample. The time dependent SH signal from the sample gives insight into the charge carrier transfer rates across the interface. By examining the dependence of these transfer rates on the incident intensity, it is possible to infer the probable processes involved.

During these experiments, the sample is irradiated with different intensities, each time starting at a virgin spot, while the evolution of the SH signal as a function of time is recorded. The polarization of the incident beam and the detected beam is P-polarized for all the measurements. The results from the virgin samples were used for comparison with results from previous studies [11].

3.4.2 Time dependent SH measurements of pre-irradiated samples

During the irradiation of Si/SiO$_2$ two distinct processes occur simultaneously. Trap sites are generated and subsequently populated. The density of trap sites eventually reaches a saturation level depending on the applied intensity. By examining the temporal evolution of the SH signal from pre-irradiated samples, it is possible to monitor only the charge trapping process, since it can be assumed that no further trap sites are created. In this fashion the two independent processes are de-convoluted.

After acquiring the data from the time dependent SH measurements described in Section 3.4.1 the beam was blocked for different dark periods. During these dark periods the background signal was still recorded, to ensure that upon recommencing of the irradiation process, the immediate SH response from the sample is recorded. This results in measurements of the SH response of pre-irradiated spots and these measurements give an indication of the role of existing defects in the SHG process and can be used to compare to those of undoped Si [100].

3.4.3 Rotational anisotropy SH measurements

Rotational anisotropy measurements are normally used to determine crystal structure and orientation. It has however been shown that these measurements can also be used to determine a change in the direction of an interfacial electric field [83, 112]. This is the purpose of the measurement described here. Rotational anisotropy SH measurements imply measuring the SH response from the sample as a function of the angle of rotation of the sample around its azimuth.

Azimuthal angular SH anisotropy measurements were recorded for both the initial SH signal ($t \leq 0.2$ s, i.e. $\leq 2 \times 10^7$ laser pulses) as well as the SH signal after saturation ($t \geq 840$ s, i.e. $\geq 7 \times 10^{10}$ laser pulses). The angular step size was chosen as $9°$ and the incident beam was displaced from the axis of rotation to ensure that each measurement was performed on a virgin sample spot. When recording the azimuthal anisotropy of the initial SH signal, the measurement was averaged over three different displacements from the axis of rotation in order to reduce the influence of sample irregularities. In view of this latter aspect, a single rotational measurement proved sufficient for the azimuthal anisotropy pattern of the saturated SH signal. Here, for each angular position the temporal SH evolution was recorded and the data points between $t = 840$ s and $t = 900$ s were averaged to extract the saturated SH signal height.

3.4.4 Charge carrier screening through resonantly enhanced two-photon absorption

It has been shown that the initial SH response from highly boron doped p+-type Si/SiO_2 does not follow the expected quadratic power law dependence on the incident intensity for incident radiation with a wavelength of 782.8 nm [11]. This was attributed to resonantly enhanced two-photon absorption within the bulk Si, which resulted in charge carrier screening of the interfacial electric field and the subsequent deviation from the quadratic power law dependence of the SH signal on the incident intensity. This two-photon resonance was probed by changing the wavelength of the incident radiation to span this resonance, in order to verify this explanation.

The initial SH signal ($t < 0.2$ s) was recorded for six different center wavelengths as a function of intensity. The six center wavelengths were chosen such that the two photon energy values fall around and on a two photon absorption resonance within Si. The center wavelengths employed, and corresponding two-photon energies, are given in Table 3.2.

For each wavelength and each subsequent intensity, three measurements,

Table 3.2: Different center wavelengths used in this study, and their corresponding two-photon energy value.

Wavelength (nm)	Two-photon energy (eV)
741.2	3.35
752.4	3.3
764.0	3.25
776.0	3.2
788.3	3.15
801.0	3.1

each on a virgin spot, were recorded of the initial SH signal from p$^+$-type Si/SiO$_2$. The average of these three measurements was taken as the initial SH response at the specific wavelength and intensity.

Each of the center wavelengths listed in Table 3.2 represent spectra with different widths. This is a result of the gain line shape of Ti:Sapphire which is non-uniform across its emission range. The laser pulses associated with each specific center wavelength therefore have slightly different pulse lengths. The pulse lengths for each center wavelength were measured and were found to be within 5% of the value obtained for the pulse length at 782.8 nm, namely 73 fs. This implies that the pulses at different wavelengths are not all transform limited but this fact should not influence the results, since it is only the incident intensity that determines the SH response from the sample. The incident intensity is only determined by the spot size (which remains nearly unchanged over this small wavelength range), the pulse length and the pulse energy.

3.5 Sample preparation and properties of p$^+$-type Si/SiO$_2$

All the samples investigated were obtained from Crystec, GmbH, Germany, and were Czochralski-grown single crystalline silicon wafers with (100) surface orientation. The as-received samples were first degreased in an ultrasonic bath with organic solvents (methanol, acetone, tri-chloroethylene), rinsed in de-ionized water before the native oxide layer was removed by treating the sample with 20% hydrofluoric acid [113, 114]. The samples were then stored under dark, normal conditions to regrow a native oxide layer (< 5 nm) [76]. All measurements were performed between 70 and 110 hours after sample preparation.

While the oxide layer is removed, the bulk Si is exposed for a short time. Any contamination during the cleaning process can during this time attach to the bulk Si. The inclusion of contaminants will strongly influence the preparation of the interface. Trapped impurities at the interface will influence the number of naturally occurring defects and the behaviour of these defects. To avoid this, extreme care has to be taken to ensure a clean environment during the cleaning process. The presence of contaminants can be easily seen in the measured SH response from the sample, as the time dependent SH traces differ considerably from those reported in this study.

All the samples investigated were strongly boron (B) doped p$^+$-type wafers with resistivity < 0.01 Ωcm. This corresponds to a doping concentration of $> 8.5 \cdot 10^{18}$cm^{-3}.

The absorption coefficient [115, 116] of Si determines the penetration depth of NIR light (at 782.8 nm) to be $\sim$11 μm. This is in strong contrast to the escape depth of the generated SH light (391.4 nm) which is only $\sim$100 nm. The native SiO$_2$ layer is transparent down to the deep UV due to its large band gap of 8.9 eV [77] and therefore allows for the effective transmission of both the fundamental and the SH light. These factors imply that SHG from the Si/SiO$_2$ system originates from either the interface or from the $\sim$100 nm Si layer below the interface through bulk effects (higher order multipole terms or EFISH).

Previous studies have determined that employing the setup described here, no significant heat accumulation occurs in the Si/SiO$_2$ interface [11]. Furthermore, care has been taken to not exceed the damage threshold for Si which is reported in literature as 10^3 GW/cm^2 for laser pulses of 90 fs at a wavelength of 620 nm [117, 118] and 10^4 GW/cm^2 for 120 fs pulses in the NIR spectral region [119]. All the intensities employed in this study were $<$ 120 GW/cm^2.

Chapter 4

Experimental results

The following chapter describes the experimental results obtained from a number of SH measurements examining the Si/SiO_2 interface using natively oxidized highly boron doped p^+-type Si. The doping concentration in all cases was $> 8.5 \cdot 10^{18} cm^{-3}$ ($< 0.01\ \Omega cm$). All measurements were performed using natively oxidized Si with (100) surface orientation from the same manufacturer (Crystec, Berlin, Germany). The samples were prepared using the method described in Section 3.5. Since the SH response from the samples shows a dependence on the rotation of the sample around its azimuth (see Section 4.3) the samples had to be orientated such that comparable measurements could be made. This was done by measuring the SH response as function of the rotational angle. All measurements were then performed at an azimuthal maximum of the initial response using incident P-polarized light and detecting P-polarized SH light. This ensured that recorded signal heights of different measurements could be compared directly to each other.

The first set of experiments investigated the time dependent SH signal from natively oxidized p^+-type Si/SiO_2. These measurements were done in order to compare to published results [11, 120] which verify the measurement and sample preparation techniques. Secondly, a systematic study of pre-irradiated natively oxidized p^+-type Si/SiO_2 was performed, examining the SH response from the sample as a function of intensity and dark time. Thirdly, the SH rotational anisotropy of natively oxidized p^+-type Si was investigated. The anisotropy patterns of both the initial response as well as the saturated response were recorded. Lastly, the initial SH response from the sample was measured using different fundamental wavelengths, as a function of incident intensity, probing a two-photon absorption resonance that exist within bulk Si [62, 87]. These results are each presented in separate sections in this chapter.

4.1 SH response from virgin p$^+$-type Si/SiO$_2$

In this section the temporal evolution of the SH signal from natively oxidized highly boron doped p$^+$-type Si/SiO$_2$ ($> 8.5 \cdot 10^{18}$cm^{-3}, < 0.01 Ωcm), prepared as described in Section 3.5, is investigated. All measurements were performed on the same sample (i.e. same doping, surface orientation (001) and manufacturer (Crystec, Berlin, Germany)).

Fig. 4.1 shows the temporal evolution of the SH signal for 6 different incident intensities ranging between 35 and 115 GW/cm^2. All curves were recorded starting with a virgin spot on the wafer. Each spot on the sample was irradiated for ∼15 min with a different intensity while the SH signal was recorded. The beam was opened ∼10 s after the start of data acquisition, ensuring that the start of the irradiation process is recorded. The solid lines in Fig. 4.1 are fitting curves according to Eq. 5.2.
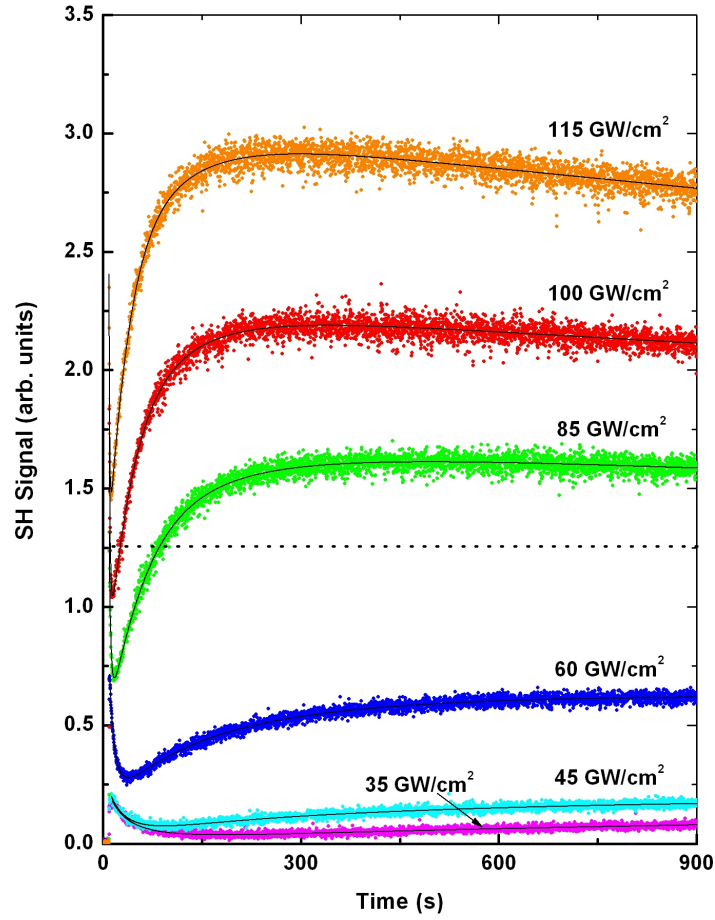
Figure 4.1: Temporal SH response of natively oxidized p$^+$-type Si/SiO$_2$ for six different intensities: 115 GW/cm^2, 100 GW/cm^2, 85 GW/cm^2, 60 GW/cm^2, 45 GW/cm^2 and 35 GW/cm^2. The solid lines are fitting curves according to Eq. 5.2.

In each of the curves, the SH intensity shows a strong initial response. This initial response increases as a function of intensity. After the initial response, the SH intensity shows a strong decline over many seconds to a local minimum, after which the signal increases over many minutes. A weak decrease, appearing on a much longer time scale, is also visible for intensities > 60 GW/cm^2.

Fig. 4.2 shows the results of the same measurement, focusing on the first 90 s of irradiation (0 - 100 s), clearly displaying the strong initial response, subsequent decline and recovery of the SH signal. The strength of the initial signal is clearly dependent on the intensity, as is the magnitude of the subsequent decline and rate of decline. The solid lines are again fitting curves

to the data according to Eq. 5.2.
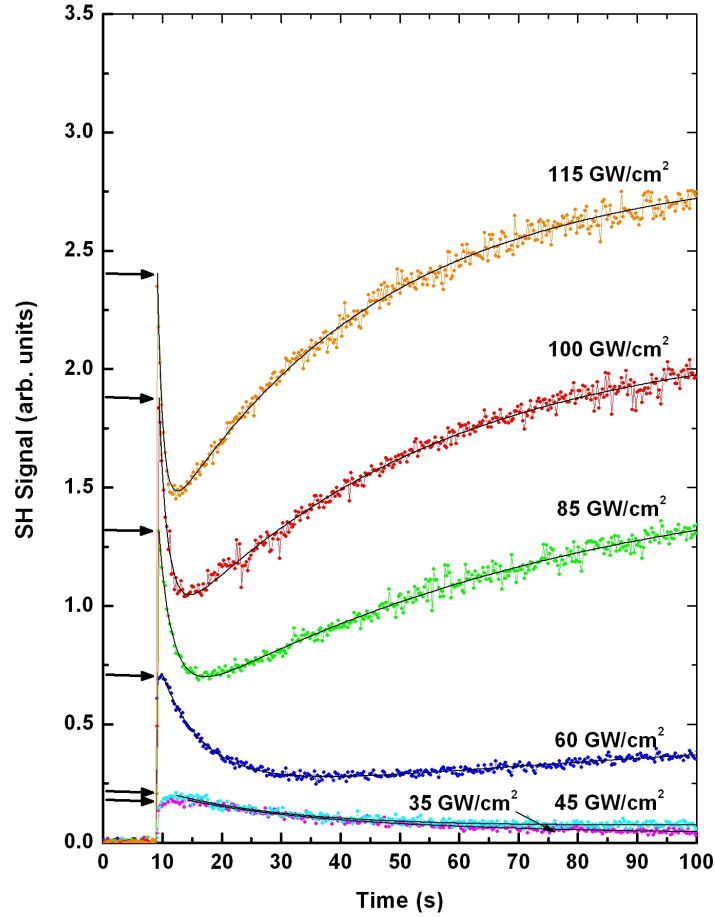
Figure 4.2: Temporal SH response of natively oxidized p$^+$-type Si/SiO$_2$ for early times (< 100 s) for six different intensities: 115 GW/cm², 100 GW/cm², 85 GW/cm², 60 GW/cm², 45 GW/cm² and 35 GW/cm². The solid lines are fitting curves to the data according to Eq. 5.2.

4.2 SH response from pre-irradiated p$^+$-type Si/SiO$_2$

The following section presents a systematic analysis of the SH response from the Si/SiO$_2$ interface of a natively pre-irradiated highly boron doped p$^+$-type Si sample ($> 8.5 \cdot 10^{18}$cm^{-3}, < 0.01 Ωcm), after varying irradiation interrupts of 10 to 600 s. The samples are initially exposed to NIR femtosecond irradiation as described in Section 4.1, after which it is given time to relax

during varying dark periods before being re-irradiated. The temporal SH response of the pre-irradiated samples are recorded and the SH response upon recommencement of irradiation is investigated.
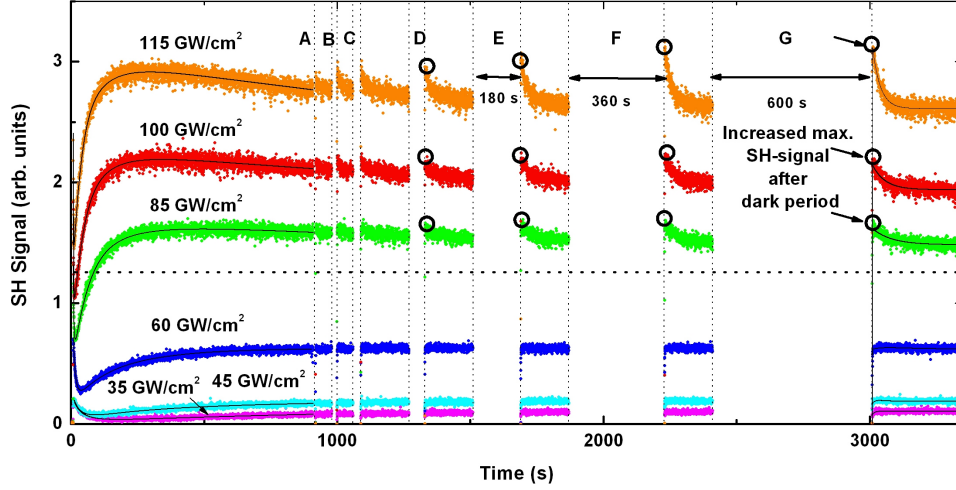

Figure 4.3: Temporal evolution of the SH signal in natively oxidized p$^+$-type Si/SiO$_2$ irradiated at various peak intensities. A-G indicate dark periods of 10 s (A), 20 s (B), 30 s (C), 60 s (D), 180 s (E), 360 s (F) and 600 s (G). The solid lines are fitting curves to the data according to Eq. 5.2.

The complete recording of the SH signal with time, including all the mentioned interrupts, for six different incident intensities (35, 45, 60, 85, 100 and 115 GW/cm^2 respectively), is shown in Fig. 4.3. The first 900 s of Fig. 4.3 is a duplicate of Fig. 4.1. After 900 s, the beam is blocked for 10 s (indicated by dashed line A), unblocked for 60 s to allow the SH signal to recover, blocked again for 20 s (indicated by dashed line B), unblocked for 60 s to allow for signal recovery, and so forth for the rest of the interrupt periods. The subsequent blocking times are (C) 30 s, (D) 60 s, (E) 180 s, (F) 360 s and (G) 600 s with irradiation times of 180 s between (D), (E), (F) and (G) to allow for complete signal recovery. The solid lines in Fig. 4.3 are fitting curves to the data according to Eq. 5.2. The re-irradiation times are chosen such that the irradiation time is long enough to transport enough charge carriers across the interface in order to obtain a steady state SH signal before the next dark period.

For intensities ≤ 60 GW/cm^2 the SH signal recovers after each interrupt to the same equilibrium value that was reached before the interrupt. This recovery occurs over many seconds, but depends on the interrupt time. For intensities > 60 GW/cm^2 the SH signal recovers to a value which is higher

than the equilibrium value obtained before the interrupt. This signal recovery, which occurs over a number of seconds and depends on the interrupt time, is followed by a decline in the SH signal over a longer period, to the previous equilibrium value. The time for this decline depends on the duration of the dark period. The circles in Fig. 4.3 are drawn to indicate the increased SH response after interrupts exceeding 60 s, as the increase is only significant after these extended interrupt periods.

Figure 4.4: Temporal evolution of the SH signal in natively oxidized p$^+$-type Si/SiO$_2$ irradiated at various peak intensities after a dark period of 600 s. The solid lines are fitting curves to the data according to Eq. 5.2.

Fig. 4.4 shows the last 350 s of the same measurement as in Fig. 4.3, i.e. the signal recovery after the last interrupt of 600 s. The solid lines are again fitting curves to the data according to Eq. 5.2. The elevated SH signal maxima and strong decline after reaching these maxima for intensities

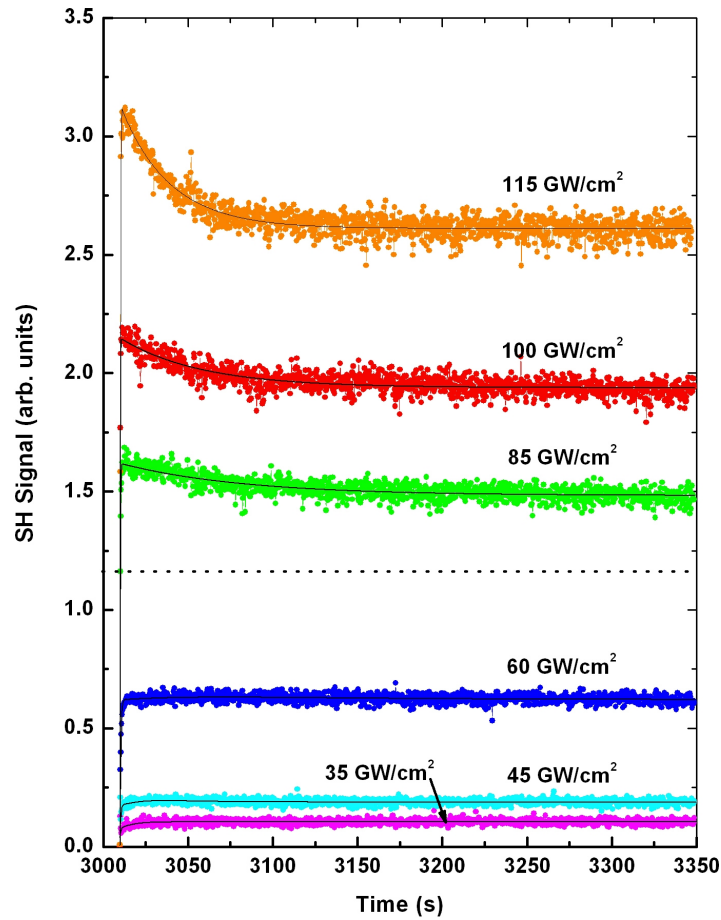> 60 GW/cm^2, is clearly visible.
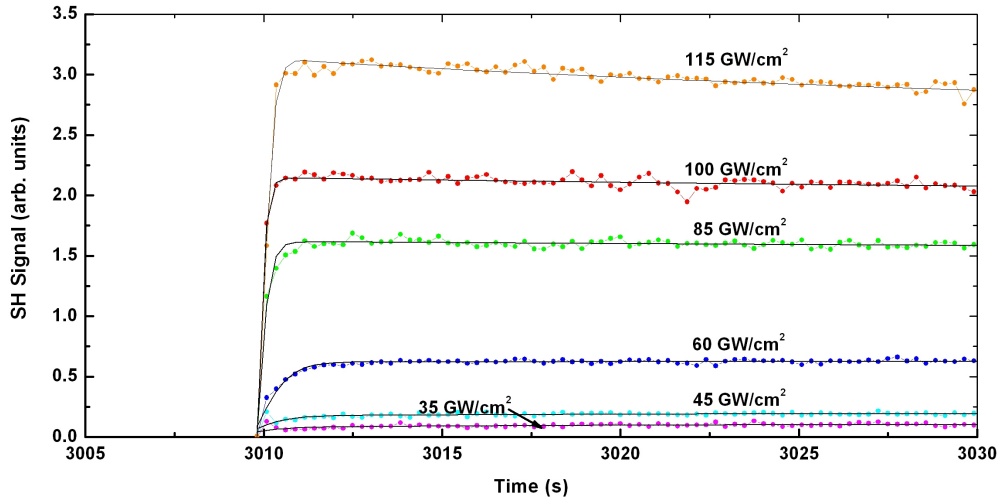
Figure 4.5: First 20 s of the temporal evolution of the SH signal in natively oxidized p$^+$-type Si/SiO$_2$ irradiated at various peak intensities after a dark period of 600 s. The solid lines are fitting curves to the data according to Eq. 5.2.

Fig. 4.5 shows the first 20 s (3010 s - 3030 s) after the recommencement of irradiation after the interrupt of 600 s. It is clear from this graph that the SH signal reaches a maximum, for all intensities, only after a couple of seconds. The time needed to reach these maxima decreases as the intensity increases. The solid lines in Fig. 4.5 are again fitting curves to the data according to Eq. 5.2.

4.3 SH rotational anisotropy measurements for p$^+$-doped Si/SiO$_2$

SH rotational anisotropy measurements are in general performed to obtain information about the crystal structure or orientation of a sample. Since it is the anisotropy of the induced nonlinear polarization which is probed, the measurement has been shown to provide information on the direction of interfacial electric fields [83, 112]. The measurement described here is a recording of the SH rotational anisotropy of the initial response (clearly seen in Fig. 4.2) from p$^+$-type Si/SiO$_2$ and the anisotropy of the saturated equilibrium SH response from p$^+$-type Si/SiO$_2$.

The azimuthal angular dependencies of the initial and saturated SH signals of highly boron doped natively oxidized p$^+$-type Si/SiO$_2$ are displayed in Fig. 4.6. Both curves show a four-fold symmetry and a phase shift of 45° relative to each other, i.e. the maxima of the initial signal corresponds to the minima of the saturated signal and vice versa. The observed phase inversion in the SH rotational anisotropy from p$^+$-type Si/SiO$_2$ purely as a result of laser irradiation is documented for the first time.
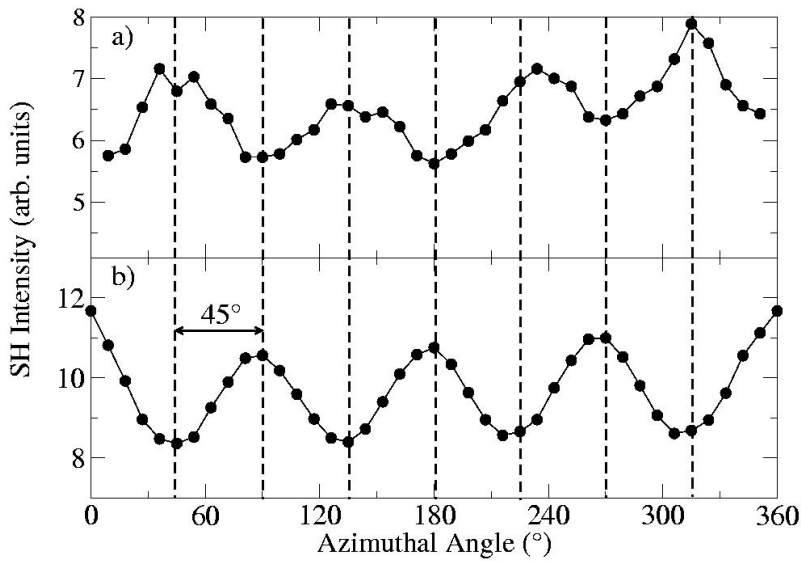
Figure 4.6: Azimuthal angular dependence's of the initial (a) and the saturated SH signals (b) recorded at 95 GW/cm^2 peak intensity when irradiating natively oxidized p$^+$-type Si/SiO$_2$.

4.4 Charge carrier screening in p$^+$-type Si/SiO$_2$ through resonantly enhanced two-photon absorption

The influence of the incident wavelength on the initial SH response from p$^+$-type Si/SiO$_2$ was investigated. The initial SH signal from natively oxidized p$^+$-type Si/SiO$_2$, as a function of incident wavelength and intensity, is plotted in Fig. 4.7 (a) - (f) as double logarithmic plots. For each of the selected center

wavelengths, the initial SH signal from the p^+-type Si/SiO_2 was recorded with the same set of incident powers and hence intensities, since the pulse lengths measured for each of the center wavelengths did not vary significantly (see Section 3.4.4). The initial SH signal for all the center wavelengths applied here show a power law dependence on the incident intensity, for all the applied intensities. The exponents of these power law dependencies however vary as a function of wavelength.
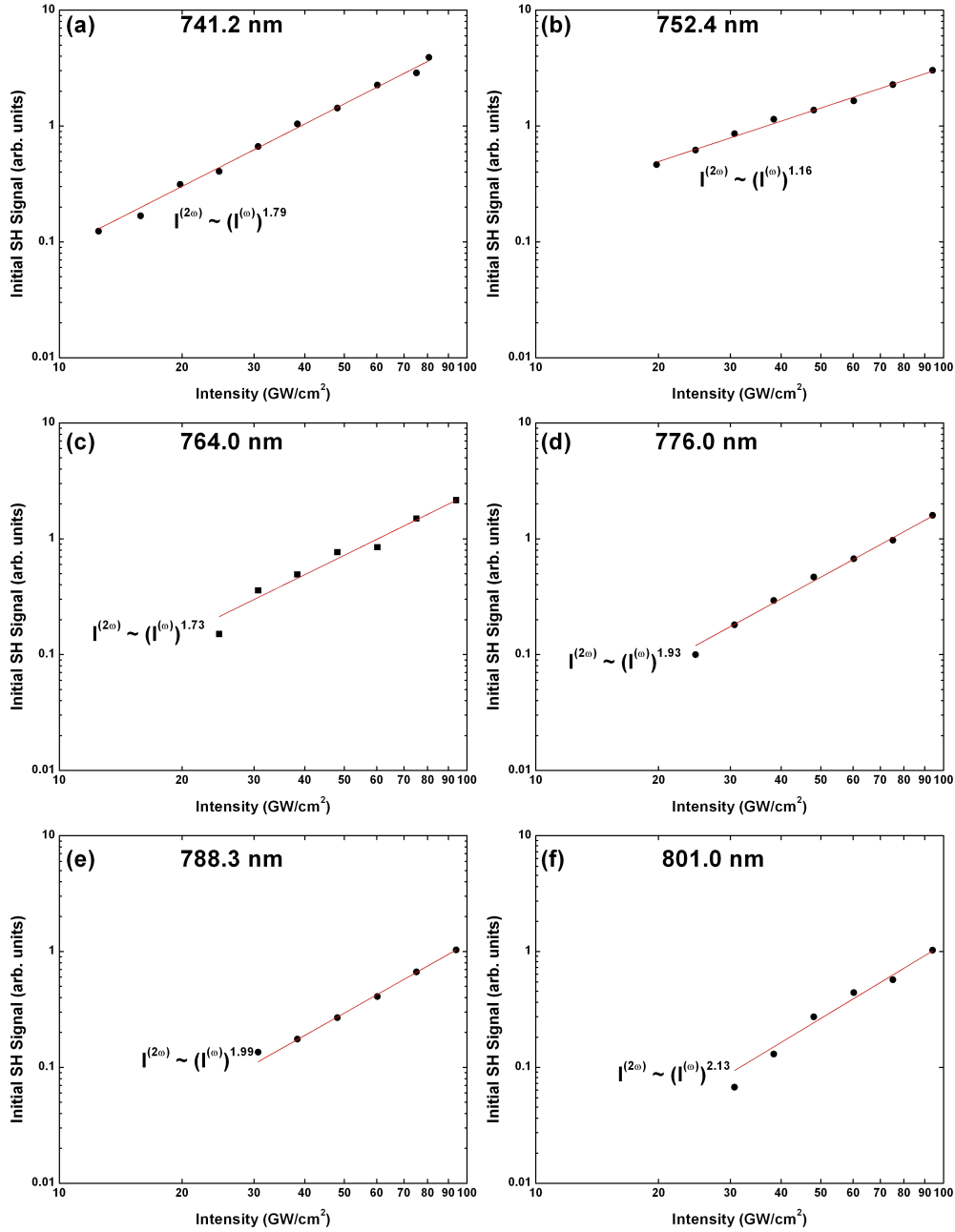
Figure 4.7: Double logarithmic plots of the initial SH signal from highly boron doped natively oxidized p$^+$-type Si/SiO$_2$ as a function of incident intensity, for six different center wavelengths, (a) - (f). The center wavelengths used, and their corresponding two-photon energies, were (a) 741.2 (3.35 eV), (b) 752.4 (3.3 eV), (c) 764.0 nm (3.25 eV), (d) 776.0 nm (3.2 eV), (e) 788.3 nm (3.15 eV) and (f) 801.0 nm (3.1 eV). The red solid lines represent fits according to a simple power law, $I^{(2\omega)} \propto \left(I^{(\omega)}\right)^n$.

Chapter 5

Discussion

In the following chapter, the experimental findings presented in chapter 4 will be discussed, using physical mechanisms previously proposed [11, 120]. The observed SH data will be interpreted using a model involving photo-induced charge transfer and subsequent trapping as well as doping induced interfacial defect ionization. This model seems to adequately explain the observed SH response from p^+-type Si/SiO_2.

5.1   SH response from virgin p^+-type Si/SiO_2

The SH response curves from natively oxidized highly boron doped p^+-type Si/SiO_2 (< 0.01 Ωcm, $> 8.5 \cdot 10^{18}$ cm^{-3}), shown in Fig. 4.1, show the same trends as those reported earlier [11, 120], despite small differences in laser parameters and inevitable changes in sample preparation.

The following explanation for the observed temporal SH trend is similar to that proposed by Scheidt [11] with the next three sections lending corroborating findings.

Fig. 5.1 represents a simplified schematic of the energy band diagram of an atomically clean, highly boron doped p^+-type Si surface [121].

In many cases of surface reconstruction, surface dangling bonds are energetically placed in the band gap [122]. Furthermore, it is well known that atomically clean Si surfaces can support electrically active defects. An example of this is interstitials that are efficiently absorbed in surface defect states which induces Fermi level (E_F) pinning and near-surface band bending [121, 122, 123]. This can establish a narrow space charge region (SCR) and subsequent internal electric field (E_0) that points into the bulk of the semiconductor (Fig. 5.1). Defect state densities in the order of 10^{10} - 10^{11} cm^{-2} are required to globally pin the Fermi level (E_F) at mid-gap [122]. In
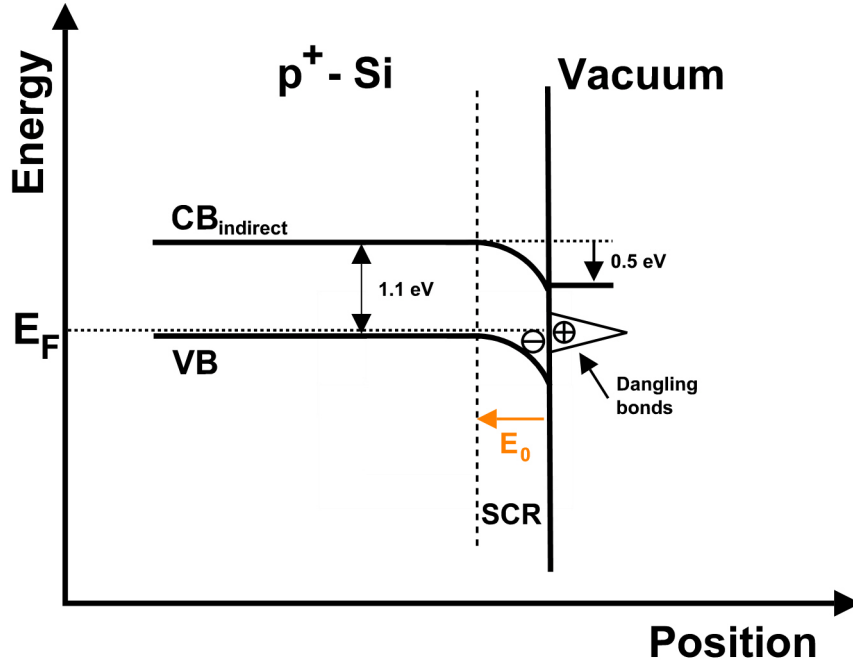
Figure 5.1: A schematic diagram of the energy band structure of atomically clean highly boron doped p$^+$-type Si, showing near-surface band bending due to positively ionized dangling bond states, Fermi level (E$_F$) pinning at mid-gap and the subsequent space charge region (SCR) and internal electric field, E$_0$.

the case of Si that has been doped with a high concentration of p$^+$-type dopants (boron in this study), the Fermi level (E$_F$) lies close to the valence band (VB) edge. In this case, band bending of ~ 0.5 eV occurs at the surface (Fig. 5.1) [114, 121, 123] which results in an internal electric field (E$_0$) which is strong enough to even change the linear optical properties of the surface [114, 124]. Since SHG is sensitive to internal electric fields, this effect should be clearly detectable by SHG [74].

It is possible, through thermal growth techniques, to prepare Si/SiO$_2$ interfaces that are virtually free of electrically active defects [114], which implies a flat band structure at the interface. In the case of natively oxidized Si/SiO$_2$ a high number of natural defects occur at the interface. Recent experiments have shown that it is possible to induce controlled amounts of bond rupture (defects) at the interface through ion-bombardment. If the Si contains a high boron doping concentration (10^{18} cm^{-3}), this leads to band bending at the interface of a comparable magnitude to that of the atomically clean surface [113, 114, 121, 123].

All the samples used in this study were natively oxidized highly boron doped p$^+$-type Si/SiO$_2$. It is assumed that, because of the uncontrolled oxidation process, a large density of incompletely saturated interface bonds exist which form interface defect states that are energetically situated within the Si band gap. It has been suggested [11, 120] that the energy band diagram of natively oxidized p$^+$- Si/SiO$_2$ looks similar to that of the atomically clean p$^+$-Si surface. The amount of band bending that occurs would be dependent on the density of the naturally occurring defects and cannot be directly determined. The energy band diagram of natively oxidized p$^+$- Si/SiO$_2$ interface should therefore look like that depicted in Fig. 5.2.

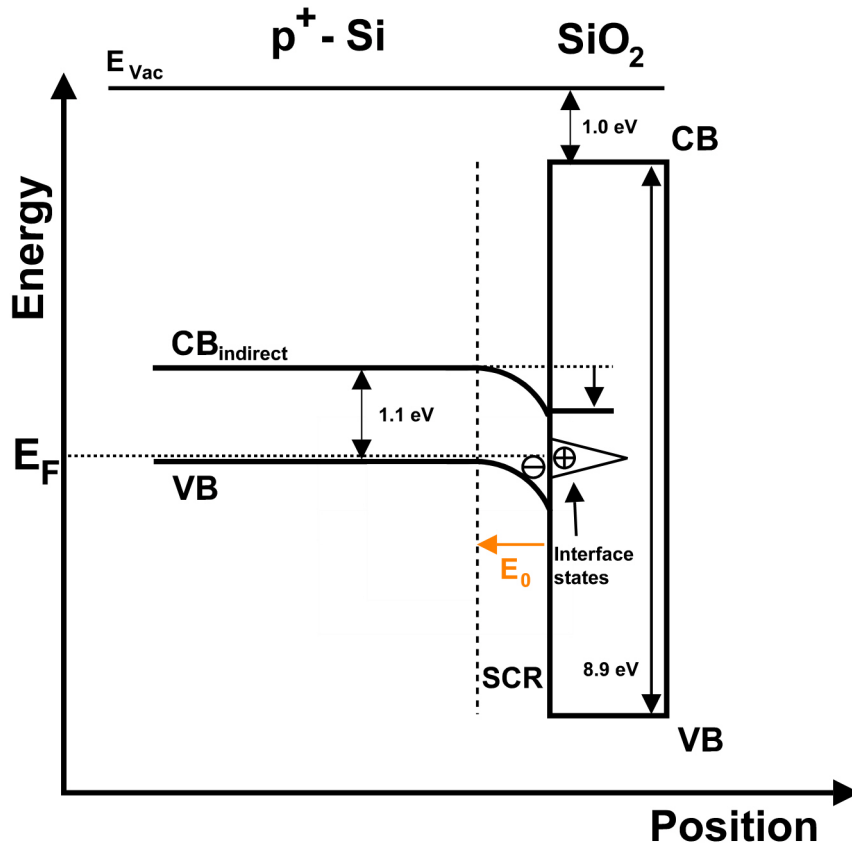Figure 5.2: Schematic energy band diagram of natively oxidized p$^+$-type Si/SiO$_2$. Positive ionization of the interface defect states leads to Fermi level (E$_F$) pinning, near-interface band bending, a narrow space charge region (SCR) and a built-in electric field (E$_0$). CB is the conduction band, VB the valence band and E$_{vac}$ the vacuum energy.

In order to obtain measurable changes in the EFISH signal originating

from the interface (Eq. 2.25) it is necessary to have interfacial charge densities in the order of $\sim 10^{11}$ cm^{-2}, which corresponds to an interfacial electric field $> 10^4$ V/m [75]. This relates to fractional interfacial defect coverages between 10^{-4} and 10^{-3}. Only at these coverages are interfacial electric fields achieved that will be detectable by SHG under the conditions applied here. These defect coverage values seem reasonable for native Si/SiO$_2$.

The considerations mentioned above lead to an explanation for the observed SH response curves in natively oxidized p$^+$-type Si/SiO$_2$ considering a superposition of electric fields as a result of electron and hole effects and taking the doping induced built-in electric field into account [11, 100]. Under NIR femtosecond radiation hot electrons are generated in the bulk Si through three-photon excitation or cascaded one- and two-photon processes. These hot electrons have sufficient kinetic energy to overcome the band offset of 4.3 eV [77] between the Si valence band and the SiO$_2$ conduction band and hence electron injection into the SiO$_2$ occurs. The resulting charge separation leads to an electric field across the interface, pointing out of the bulk Si. If the incident laser intensity is high enough to induce multi-photon processes [11, 100] it is possible to induce hole injection into the SiO$_2$ from the bulk Si. Hole injection has a energy barrier of 5.7 eV [77] implying that a four-photon process is necessary for the holes to surmount this energy barrier. In undoped natively oxidized Si/SiO$_2$ the contributions from holes only become significant at intensities > 45 GW/cm^2. The contribution of injected holes to the nett electric field is delayed due to the lower cross-section of a four-photon process compared to a three-photon process as well as the lower mobility of holes compared to electrons in Si. This difference in charge transfer rates can be seen even more clearly in the SH response from a pre-irradiated sample (Fig. 4.4, explained in Section 5.2). The superposition of these three contributions to the nett interfacial electric field is shown in Fig. 5.3 which depicts a schematic energy band diagram of p$^+$-type Si/SiO$_2$ under NIR femtosecond irradiation.

Fig. 5.3 (a) is a schematic of the energy band diagram of natively oxidized highly p-doped Si showing the superposition of the built-in doping related electric field E$_0$ and the opposing photo-induced electric field as a result of electron transfer and trapping at the interface, E$_{el}$. Fig. 5.3 (b) shows the added effect of hole transfer and trapping in the oxide and the subsequent electric field, E$_h$, that results at intensities in this study > 60 GW/cm^2. The experimental traces that are observed in Fig. 4.1 are superpositions of these three (E$_0$, E$_{el}$ and E$_h$) contributions to the interfacial electric field according to Eq. 2.25.

It is therefore possible, with the doping induced built-in electric field as a starting condition and then including the superposition of the photo-induced
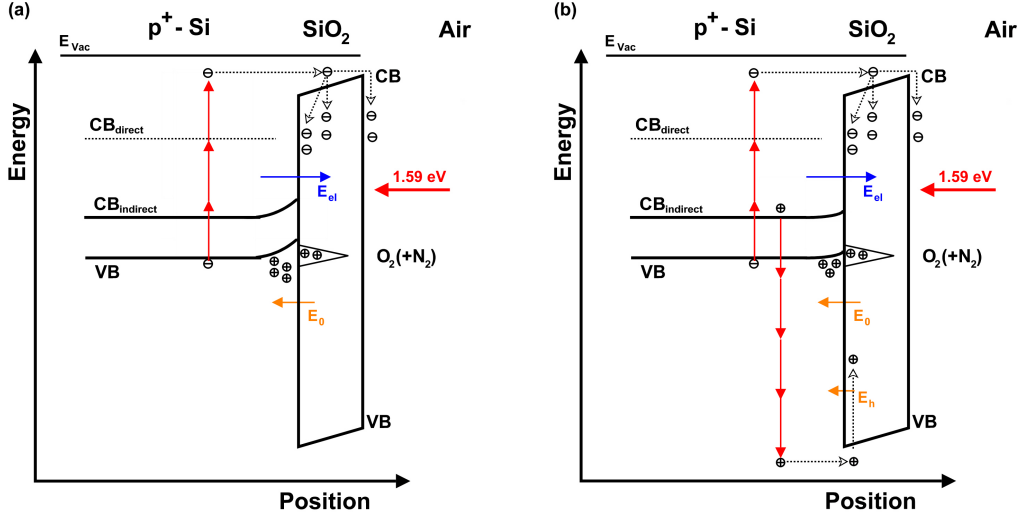
Figure 5.3: Schematic band diagrams of native p$^+$-type Si/SiO$_2$ interface under NIR femtosecond laser irradiation. Schematic (a) shows a superposition of the doping induced electric field (E$_0$) and the photo-induced electric field which results from electron transfer and trapping (E$_{el}$). Schematic (b) includes the weaker effect of photo-induced hole transfer and trapping (E$_h$) which only become significant at higher intensities. The nett electric field is a superposition of all three effects and the resultant SH signal probes this nett electric field (Eq. 2.25).

electron and hole related electric fields, to explain all the effects observed in the transient SH signals (Fig. 4.1) obtained from natively oxidized highly boron doped p$^+$-type Si/SiO$_2$.

    As an example of the transient SH response curves from p$^+$-type Si/SiO$_2$, Fig. 5.4 shows the temporal SH signal recorded at 115 GW/cm^2, taken from Fig. 4.1. Upon the start of the laser irradiation, an instantaneous SH signal (EFISH) is observed as a result of the doping induced built-in electric field, E$_0$, which points into the bulk Si. A decline in the SH signal is subsequently observed as photo-induced electron transfer and trapping sets up an electric field, E$_{el}$, that opposes the built-in electric field until a local minimum is reached. This local minimum is non-zero and amounts to $\sim 55\%$ of the saturated SH signal (Fig. 4.1 and 5.4). It should be noted that if the nett electric field across the interface was zero, the SH signal should also drop to zero as it is assumed that the field-independent contributions to the SH signal are negligible under the applied conditions. The non-vanishing SH signal is thus attributed to an incomplete cancellation of the competing interfacial electric field contributions, E$_0$ and E$_{el}$. This incomplete cancellation is explained
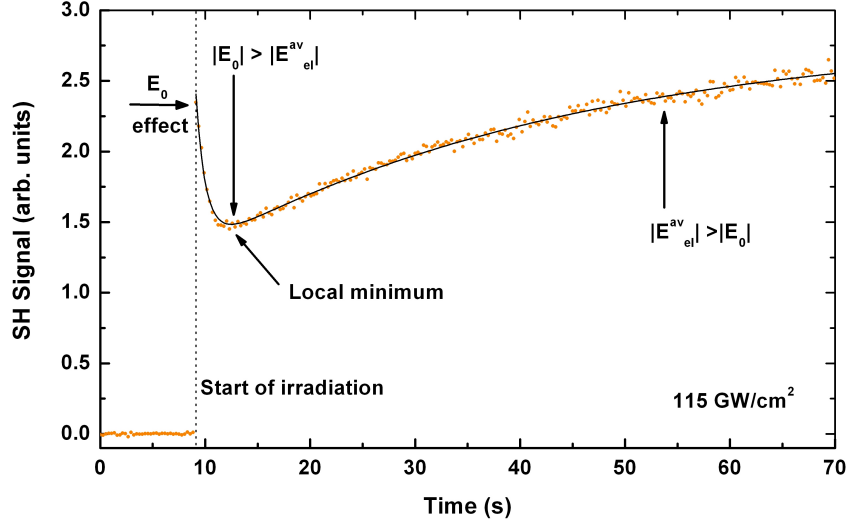
Figure 5.4: Temporal SH response curve of p$^+$-Si/SiO$_2$ from Fig. 4.1 recorded at 115 GW/cm^2; instantaneous SH signal due to doping induced built-in electric field E$_0$, superposition with electric field E$_{el}$ induced by electron transfer into SiO$_2$.

considering the spatial functionalities of E$_0$ and E$_{el}$ [120]:

It is realistic to assume a Gaussian function of $1/e$-width w_0 for the spatial envelope of the fundamental laser intensity (see Section 3.3). Since SHG is a second order nonlinear process, it can be realistically assumed that it mainly takes place in the beam center characterized by a Gaussian SHG envelope function of $1/e$-width $w_0/\sqrt{2}$. Since E$_0$ results from a uniform distribution of dopants, it can be assumed to be spatially uniform within the SHG-envelope ($w_0/\sqrt{2} \approx 4.9$ μm) and to remain nearly constant within the irradiation time [120]. The electron injection process responsible for the build-up of E$_{el}$ is mainly driven by a third order optical process [76, 77, 78]. This implies that E$_{el}$ is mainly induced within a Gaussian spatial envelope of $1/e$-width $w/\sqrt{3}$ ($< w/\sqrt{2}$) that is narrower than the SHG envelope. If one thus considers the spatial functionalities of E$_0$ and E$_{el} = E_{el}(t, x, y)$ it is apparent that the superposition of these two electric field components can never result in a zero nett interfacial electric field E$(t, x, y) = E_0 - E_{el}(t, x, y)$ for all positions (x, y) within the SHG envelope. It can therefore be seen, especially since the SH signal is independent of the sign of the nett interfacial electric field (absolute square in Eq. 2.25), that the SH signal should deviate significantly from zero at its minimum during its temporal evolution. This can be confirmed by evaluating the spatial integral

$$\int I^{(2\omega)}(t)dxdy = \int \left|\chi^{(3)}\mathrm{E}(t,x,y)\right|^2 \cdot \left(I^{(\omega)}(x,y)\right)^2 dxdy \qquad (5.1)$$

This integral is consistent with Eq. 2.25 and proves to be significantly non-vanishing for realistic ratios of $\mathrm{E}_0/\mathrm{E}_{\mathrm{el}}$ when the spatial functionalities of the respective field components are taken into account.

Two further observations can be made from the experimental SH traces of Fig. 4.1. One is that the increase in the SH signal as a result of electron transfer and trapping occurs on a much delayed time scale to that of undoped Si/SiO$_2$ [11, 100]. Secondly, the decrease in the SH signal after reaching a maximum is reduced in both magnitude and speed in natively oxidized highly boron doped p$^+$-type Si/SiO$_2$ (Fig. 4.1) compared to that of undoped Si/SiO$_2$. This second effect is an apparent consequence of the built-in electric field [11, 120]. The positive ionization of a significant density ($> 10^{11}$ cm^{-2}) of interface defect states in native p$^+$-type Si/SiO$_2$ before the start of irradiation, seems to hamper the laser induced hole trapping at the interface, since a large number of trap sites that would otherwise be available for hole trapping, are already ionized. This leads to a less pronounced decline towards equilibrium in the observed SH signal for intensities > 60 GW/cm^2 for p$^+$-type Si/SiO$_2$ than for undoped Si/SiO$_2$ [11, 100]. This can be further rationalized by assuming that photo-induced hole trapping and doping related ionization of interface defect states are competing processes that both involve trap sites that are located near the Si/SiO$_2$ interface.

The experimental time dependent SH traces observed in Fig. 4.1 can numerically be reproduced on the basis of an empirical model first introduced by Mihaychuk *et al.* [76, 77] and expanded on by Scheidt *et al.* [11, 100] to include hole effects and the built-in doping induced electric field. The following relation consists of a constant parameter $a_0 > 0$ which takes the built in electric field into account and four exponential functions that account for the electron and hole effects.

$$I^{(2\omega)} \propto \left(a_0 + \sum_{i=1}^{4} a_i \exp(-t/\tau_i)\right)^2 \qquad (5.2)$$

By using this relation with a_1, $a_4 > 0$ and a_2, $a_3 < 0$, the time-dependent traces of Fig. 4.1 are accurately reproduced (The solid lines in Fig. 4.1 are produced using this empirical model.). Fig. 5.5 shows the time constants, τ_i, in a double logarithmic plot as extracted from the numerical fits to the data versus the incident peak laser intensity. The time constants are also listed in Table 5.1. The time constant τ_1 describes the initial decline in the observed SH signal ($a_0 > 0$) after the instantaneous SH signal in Fig. 4.1 and follows

the power law $1/\tau_1 \propto I^{n_1}$ (Fig. 5.5). The exponent $n_1 = -3.05(\pm0.23)$ is similar to that reported earlier ($n_1 = -2.9$ [11]) and is very similar to the exponent found for undoped samples. The value of $n_1 = -3.05$ indicates a three-photon process and supports the explanation that the decrease in SH signal after the initial signal is a result of electron transfer and trapping in the SiO$_2$ layer that creates an electric field E$_{el}$ that opposes the built-in electric field E$_0$.

Table 5.1: Time constants τ_i for the temporal SH evolution as a function of the incident laser peak intensity I extracted from the numerical data fits for native p$^+$-type Si/SiO$_2$.

Intensity (GW/cm^2)	τ_1 (s)	τ_2 (s)	τ_3 (s)	τ_4 (s)
35	~ 60	~ 370	~ 3200	-
45	32 ± 7	~ 130	~ 1050	-
60	9.3 ± 0.6	87 ± 27	~ 260	-
85	2.7 ± 0.13	49 ± 8	~ 150	~ 32310
100	1.7 ± 0.09	32 ± 3	~ 93	~ 23900
115	1.0 ± 0.06	26 ± 1	~ 91	~ 11300

The time constant τ_4 describes the slow signal decrease ($a_4 > 0$) over a period of many minutes at high incident peak intensities (> 60 GW/cm^2). τ_4 follows the power law $1/\tau_4 \propto I^{n_4}$ (Fig. 5.5). The exponent $n_4 = -2.92(\pm0.88)$ is close to that reported earlier ($n_4 = 3.2$ [11]). The value of τ_4, although maybe not apparent from these measurements unless the error margin is taken into account, supports the notion of a four-photon process and hence hole injection and trapping in the SiO$_2$ layer. The deviation from a pure fourth order intensity dependence is attributed to cascaded multiple one-, two- and three-photon processes [100, 120].

The dependence of the time constants τ_2 and τ_3 on the intensity was also fitted according to a simple power function. As can be seen from Fig. 5.5 the fit to the data for these two time constants is not very accurate. If one examines the extracted exponents ($n_2 = -3.07(\pm0.46)$ and $n_3 = -4.48(\pm0.21)$), τ_2 does seem to indicate a three-photon process and τ_3 a four-photon process. Since the fit to the data is not conclusive, this cannot be stated with confidence. This implies that the empirical model described fails to conclusively attribute any defined processes to these two time constants and shows the limitations of the model. This is similar to what was found in earlier measurements [11]. The model does however reproduce the experimental curves (Fig. 4.1) very accurately and supports the notion of doping related ionization of the interface defect states (E$_0$) and subsequent charge dynamics

and trapping (E$_{el}$ and E$_h$) in the SiO$_2$ layer under NIR femtosecond irradiation. The correlation between these measurements, along with the extracted time constants, and measurements that were performed previously [11, 120] supports the reproducibility of these and subsequent measurements.

Figure 5.5: A double logarithmic plot of the time constants τ_i as extracted from the numerical fit to the data in Fig. 4.1 using Eq. 5.2.

5.2 SH response from pre-irradiated p$^+$-type Si/SiO$_2$

The observed time dependent SH response from pre-irradiated natively oxidized p$^+$-type Si/SiO$_2$, shown in Figs. 4.3 - 4.5, displays a unique temporal behaviour. This temporal SH response from pre-irradiated native p$^+$-type Si/SiO$_2$ is reported for the first time. Similar to what was observed in the case of undoped Si/SiO$_2$ [11, 100], the temporal SH evolution of pre-irradiated native p$^+$-type Si/SiO$_2$ shows an accelerated dynamic behaviour upon re-irradiation after dark periods A to G in Fig. 4.3 compared to the temporal SH signal from virgin native p$^+$-type Si/SiO$_2$. Unlike the case of undoped Si/SiO$_2$, the SH signal from pre-irradiate native p$^+$-type Si/SiO$_2$ upon re-irradiation takes longer than the temporal resolution of the experiment (0.2 s) to reach a maximum for all the intensities applied here. The time

taken to reach the respective maximum decreases with increasing intensity. For intensities ≤ 60 GW/cm^2 the SH signal takes a number of seconds before reaching an equilibrium value approximately the same as before the interrupt. For intensities > 60 GW/cm^2, the SH signal increases to a maximum that is higher than the equilibrium value before the interrupt, before rapidly decreasing to the previously established equilibrium value. The magnitude of this enhanced SH signal amplitude (empty circles in Fig. 4.3) increases with the duration of the dark period up to approximately 600 s. The subsequent SH signal decrease takes place on a much accelerated time scale compared to the decrease experienced from virgin samples. The increase in SH signal is however much less pronounced than was found for pre-irradiated undoped native Si/SiO$_2$ [11, 100]. The decline after reaching a maximum is also not as swift in the case of pre-irradiated native p$^+$-doped Si/SiO$_2$ as was seen with pre-irradiated native undoped Si/SiO$_2$ [11, 100].

The SH response from pre-irradiated native highly boron doped p$^+$-type Si/SiO$_2$ is reproduced following a straight forward approach using Eq. 5.2. This takes into account the fact that the initial electric field E$_0$ still exists across the interface. For intensities ≤ 60 GW/cm^2 Eq. 5.2 is used with $a_3 = a_4 = 0$ since hole effects play no noticeable part at these low intensities. The extracted time constants τ_i^p for the pre-irradiated samples are shown in Table 5.2.

Table 5.2: Time constants τ_i^p for the temporal SH evolution as a function of the incident laser peak intensity I extracted from the numerical data fits for pre-irradiated native p$^+$-type Si/SiO$_2$.

Intensity (GW/cm^2)	τ_1^p (s)	τ_2^p (s)	τ_3^p (s)	τ_4^p (s)
35	0.84 ± 0.004	0.84 ± 0.007	-	-
45	0.87 ± 0.005	0.87 ± 0.006	-	-
60	0.64 ± 0.05	0.64 ± 0.05	-	-
85	~ 0.18	~ 0.18	~ 63	~ 63
100	~ 0.12	~ 0.12	~ 48	~ 48
115	~ 0.24	~ 0.22	~ 29	~ 29

All four time constants τ_i^p ($i = 1 \ldots 4$) are orders of magnitude smaller than those for virgin samples, confirming the observed trend of accelerated charge dynamics. Furthermore, it is worth noting that τ_1^p has very similar values to τ_2^p while τ_3^p and τ_4^p are also alike for all intensities. Since $\tau_1^p \simeq \tau_2^p$ and $\tau_3^p \simeq \tau_4^p$, only τ_1^p and τ_3^p are plotted versus intensity in Fig. 5.6. All four time constants τ_i^p ($i = 1 \ldots 4$) have values that are noticeably larger than the corresponding time constants found for pre-irradiated undoped Si/SiO$_2$

[11, 100]. This indicates delayed electron and hole dynamics in the case of pre-irradiated p$^+$-type Si/SiO$_2$ compared to pre-irradiated undoped Si/SiO$_2$.
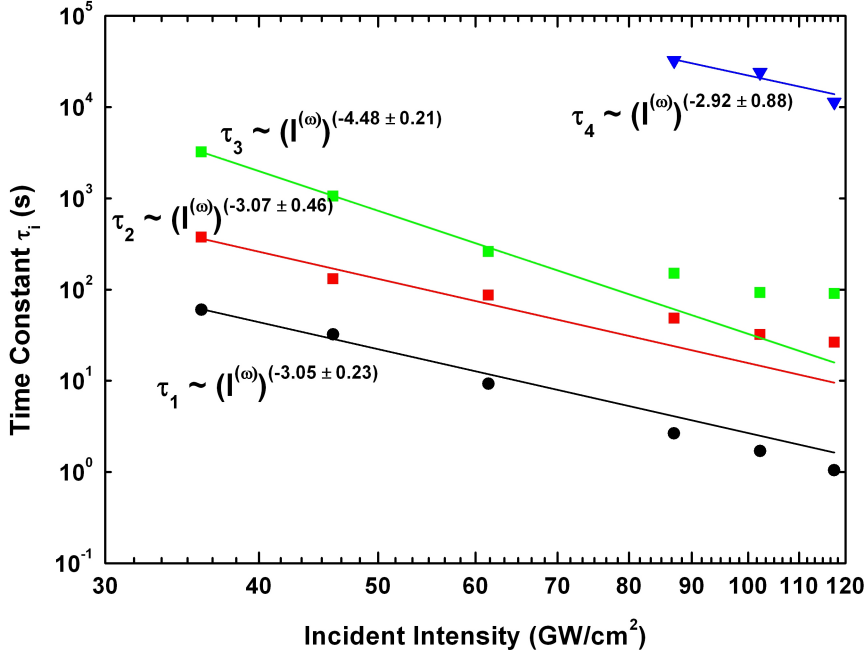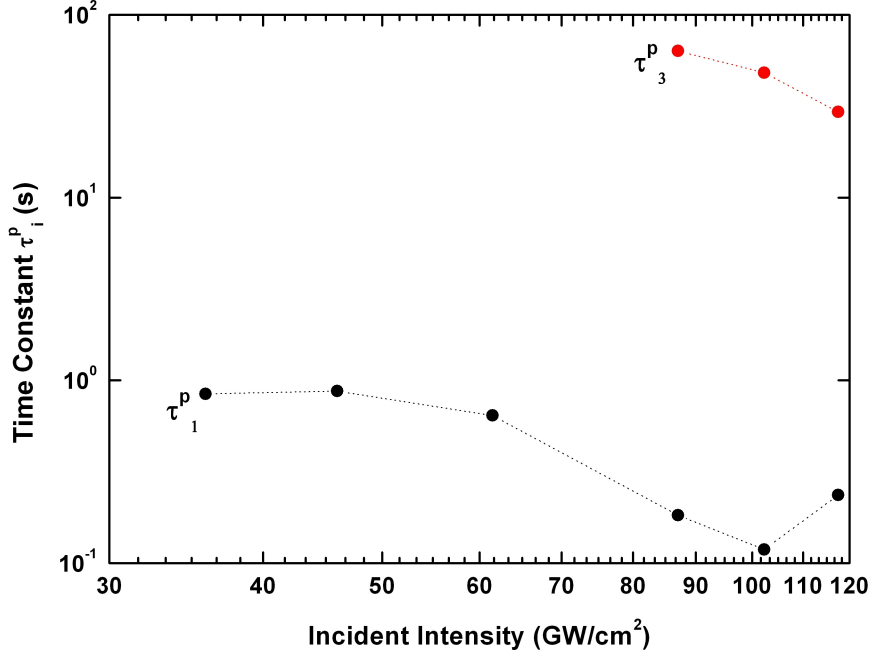

Figure 5.6: A double logarithmic plot of the time constants τ_1^p and τ_3^p as extracted from the numerical fit to the data in Fig. 4.1 using Eq. 5.2. The dotted lines are merely to guide the eye.

From Fig. 5.6 it is clear that the time constants τ_i^p show complex non-monotonic intensity dependencies, which are not easily attributed to defined multi-photon processes. This indicates that the simple numerical model (Eq. 5.2) used to describe the SH behaviour of virgin samples to a degree, is inadequate in describing the behaviour from pre-irradiated samples.

The accelerated electron and hole dynamics in pre-irradiated samples compared to virgin samples can be explained, analogously to the case of undoped native Si/SiO$_2$ [11, 100], by considering the photo-induced trap generation at the Si/SiO$_2$ interface under NIR femtosecond laser irradiation. A proposed schematic energy band diagram, including photo-generated electron and hole trap sites, for pre-irradiated native p$^+$-type Si/SiO$_2$ under NIR femtosecond irradiation is shown in Fig. 5.7.
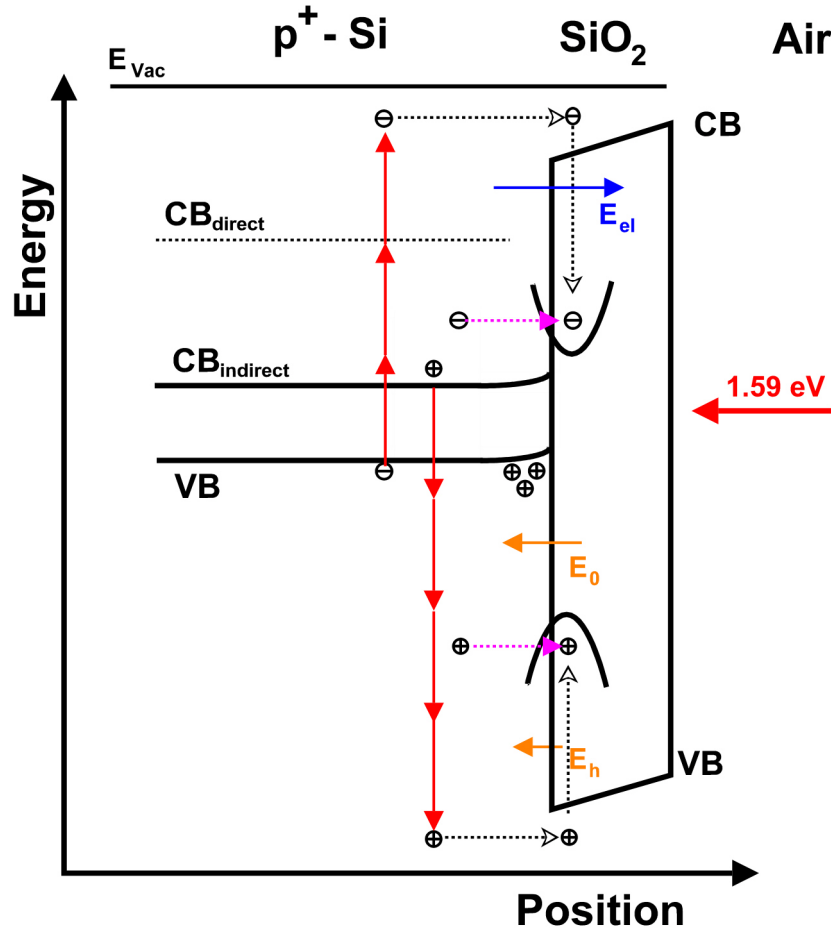
Figure 5.7: A schematic band diagram for the pre-irradiated native p$^+$-type Si/SiO$_2$ interface under NIR femtosecond laser irradiation showing photo-generated electron and hole trap sites located close to the Si/SiO$_2$ interface. The dashed blue arrows indicate proposed direct population mechanisms.

The photo-induced trap generation presumably occurs due to hot electrons and holes, which upon injection into the SiO$_2$ layer, have excess kinetic energy. These photo-generated trap sites show characteristics that differ from the naturally occurring defects present in natively oxidized Si/SiO$_2$. It is assumed that these photo-generated trap sites are located close to the Si/SiO$_2$ interface and are at relatively low energetic levels. Furthermore it is proposed that these photo-generated trap sites have different cross-sections as well as de-trapping times to the native naturally occurring trap sites at the interface.

These assumptions, along with the proposed band structure of pre-irradiated

native p$^+$-type Si/SiO$_2$, explain the accelerated charge kinetics across the interface upon re-irradiation with NIR femtosecond radiation. A large density of photo-generated trap sites (both for holes and electrons) is present upon recommencing of the irradiation process. This leads to accelerated charge carrier separation processes which is reflected in the change in time constants between virgin and pre-irradiated samples. The breakdown of the power law dependencies of the time constants τ_i^p (Fig. 5.6) for pre-irradiated samples can be taken as indications that direct photo-induced population mechanisms (dashed blue arrows in Fig. 5.7) as means of populating the photo-induced trap sites play an important role in the charge separation process of pre-irradiated samples. This direct population of trap sites dominates the normal multi-photon contribution and is responsible for the accelerated behaviour that can be seen from the pre-irradiated samples. This explanation seems plausible considering the assumed low energy values of the photo-induced trap sites as well as their proximity to the Si/SiO$_2$ interface.

5.3 SH rotational anisotropy measurements for p$^+$-type Si/SiO$_2$

The form of the SH rotational anisotropy patterns recorded from boron doped natively oxidized p$^+$-type Si/SiO$_2$ shown in Fig. 4.6 provides a verification of the model used to explain the observed temporal SH response from virgin p$^+$-type Si/SiO$_2$ described in Section 5.1. The rotational anisotropy patterns of the initial SH response and that of the saturated SH response from highly boron doped natively oxidized p$^+$-type Si/SiO$_2$ both show a four-fold symmetry but with a relative 45° phase shift between them. Two groups have previously independently studied phase shifts in the rotational anisotropy pattern of Si/SiO$_2$. The groups of Dadap *et al.* [83, 112] studied the SH response from MOS devices with externally applied DC voltages. They recorded a four-fold SH anisotropy pattern from the device under investigation when large external voltages were applied. When they reversed the voltage polarity, they observed a 45° phase shift in the SH anisotropy pattern originating from the MOS-device under examination. They attributed this phase shift to a reversal of the direction of the applied electric field.

    An and Cundiff examined the SH anisotropy response from Si for different incident wavelengths and different surface terminations. They also observed the above mentioned 45° phase shift in the four-fold anisotropy pattern from Si, but dependent on the incident frequency of the the fundamental light [68] as well as the surface termination [125]. The 45° phase shift as a function

of the photon energy is ascribed to the presence of resonances in the surface contribution. This is because the phase is actually a relative phase between the surface and bulk contributions, and hence, the resonance must be a pure surface state that does not originate from the bulk band structure. These surface resonances have been described in earlier spectroscopic studies [61].

Both groups worked with incident intensities below that necessary to induce significant EFISH effects ($\sim$ 2 orders of magnitude smaller than in this study). Since the measurement described here employed only a single wavelength for the fundamental, and intensities high enough to induce significant electric fields across the Si/SiO$_2$ interface, the explanation of Dadap *et al.* [83, 112] is followed, where large electric fields were present across the interface, and the phase shift in the anisotropy pattern was attributed to a change in the direction of the applied electric field (curvature of band bending).

The anisotropy patterns (Fig. 4.6) measured here show comparable behaviour, both in the amplitude of the anisotropy pattern as well as the observed phase shift, to that measured by Dadap *et al.* [83, 112]. Looking at part (a) of Fig. 4.6, the maxima of the SH signals are observed at the (relative) azimuthal angles of 45°, 135°, 225° and 315°. These same angles are the positions of the SH signal minima in Fig. 4.6 (b). The SH signal in part (a) of Fig. 4.6 represents the virgin sample with the Electric field E$_0$ induced by p$^+$-doping of the Si sample and directed into the bulk of the Si sample. The SH signal in Fig. 4.6 (b), on the other hand, represent the SH response from the sample with the nett electric field across the interface dominated by E$_{el}^{av}$, which is obtained after prolonged electron (and to a lesser degree holes) injection into the SiO$_2$ layer. This field has an opposite sign relative to E$_0$. This observation can be compared to the findings and interpretations of Dadap *et al.* [83, 112], where the reversal in the sign of the externally applied electric field was held responsible for the observed phase shift in the anisotropy pattern.

This induced phase shift in the SH anisotropy pattern supports the interpretation that the doping related and electron induced interfacial field components E$_0$ and E$_{el}$ have opposite signs and represent competing contributions to the temporal SH evolution observed in p$^+$-type Si/SiO$_2$ (Figs. 4.1, 4.2 and 5.4).

5.4 Charge carrier screening in p$^+$-type Si/SiO$_2$ through resonantly enhanced two-photon absorption

The dependence of the magnitude of the initial SH response from p$^+$-type Si/SiO$_2$ on the incident intensity varies as a function of the incident wavelength. This can be seen in Fig. 4.7 which shows the initial SH response as a function of intensity for six different wavelengths. From Eq. 2.25 a quadratic dependence of the initial SH signal on the incident fundamental intensity is expected. These measurements deviate from this quadratic dependence, as can be seen in Fig. 4.7 and summarized in Table 5.3. The measurements for all the center wavelengths applied here show a simple power law dependence, with no deviation from the power law at higher intensities, as have been reported earlier [11, 120]. The deviation from the expected quadratic power law is not attributed to limitations in the temporal resolution of the experiment, as previous measurements have shown that the time resolution of the experimental setup is sufficient to ensure the accurate recording of the initial SH signal [11, 120].

Table 5.3: Summary of incident wavelengths, corresponding two-photon energies and exponents of the power law dependence of the initial SH signal as a function of intensity for different wavelengths.

Incident center wavelength (nm)	Two-photon energy (eV)	Exponent
741.2	3.35	1.79 ± 0.11
752.4	3.3	1.16 ± 0.04
764.0	3.25	1.73 ± 0.11
776.0	3.2	1.93 ± 0.06
788.3	3.15	1.99 ± 0.05
801.0	3.1	2.13 ± 0.16

It has been suggested that the deviation from the quadratic intensity dependence of the SH signal, seen in Fig. 4.7, is due to photo-induced charge carrier screening [11, 120, 126] of the doping induced built-in electric field E$_0$. The E$_1$ direct interband transition within Si has an energy value of 3.3 eV [62, 87]. This corresponds to the two-photon energy of a laser beam with a center wavelength of 752.4 nm. Two-photon absorption at this wavelength is therefore resonantly enhanced. The other center wavelengths used in this study were chosen such that their corresponding two-photon energies lie close to this two-photon resonance (see Table 5.3). The enhancement of the two-

photon absorption, experienced by light with a center wavelength of 752.4 nm, will decrease sharply for light with a center wavelength that is far away from this resonance. The enhanced two-photon absorption on resonance leads to enhanced screening of the interfacial electric field by charge carriers. This screening of the electric field leads to a deviation from the expected quadratic dependence of the initial SH response on the incident intensity. This effect is clearly illustrated in Fig. 5.8 where the value of the exponent of the power law dependence of the initial SH signal on the incident fundamental intensity was plotted as a function of the two photon energy of the incident center wavelength. The broad nature of the two-photon resonance peak can be attributed to the broad spectrum of the incident fundamental laser pulses.
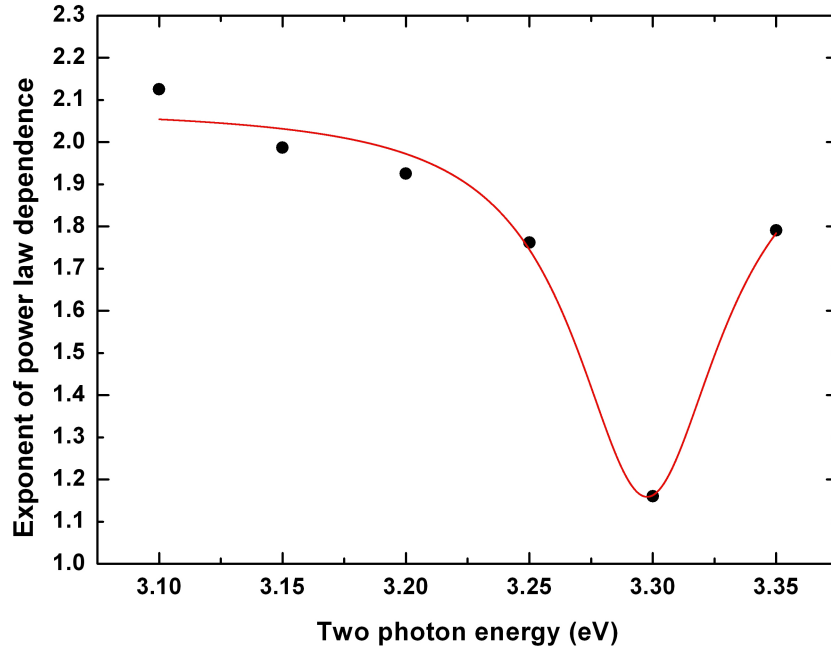
Figure 5.8: The dependence of the exponent in the power law dependence of the initial SH signal on the incident fundamental intensity, as a function of two-photon energy. The red line represents a Lorentzian fit to the data.

Upon laser irradiation, a large density of ($> 10^{17}$ cm^{-3}) [11] of electron hole pairs is photo-generated in Si over an absorption depth of < 30 μm at the NIR frequencies applied in this study. Since an electric field is always present across the interface as a result of the doping induced ionization of the interface defect states, the photo-generated electrons and holes start to separate, with the electrons being attracted to the ionized defect states. The movement of the electrons towards the ionized defect states results in

a photo-induced screening of the doping induced interfacial electric field E$_0$. This screening will occur on a timescale which is inversely proportional to the the plasma frequency ω_p of the electron-hole plasma [126]. This implies that it is an ultra-fast effect and is therefore completely distinct from the electron and hole transfer across the interface and subsequent trapping (EFISH effects) which occur on the multi-second or multi-minute timescales. Since the charge carrier screening process occurs on a time scale that is orders of magnitude shorter than the experimental resolution of the experiment (0.2 s), the observed initial SH signal is always that originating from a screened built-in interfacial electric field E$_0$. By screening the electric field E$_0$, the distance over which the interfacial electric fields acts is reduced. Since the observed SH signal only originates from the volume where an electric field is present, the observed EFISH signal is weaker since the volume that contributes to the EFISH signal is smaller [11, 120]. The amount of screening that occurs depends on the number of electron-hole pairs, and hence on the intensity of the fundamental laser irradiation. In this study however, the proportionate screening seems to increase in a very systematic and well defined way with an increase in intensity, resulting in a strict power law dependence of the initial SH intensity on the incident intensity. This dependence varies only with wavelength and hence the overlap of the incident spectrum with the two-photon energy resonance in Si.

The above argument for charge carrier screening being responsible for the non-quadratic dependence of the initial SH signal on the incident fundamental intensity is supported by a recent study by Fomenko *et al.* [127]. They observed a non-quadratic SH signal dependence on the fundamental laser intensity from the buried interface between Si$_{0.9}$Ge$_{0.1}$and its oxide. This effect is not doping related but supports the interpretation that charge carrier induced screening can severely perturb the intensity dependence of the observed SH signal. This is especially true if the creation of electron-hole pairs by two-photon absorption is resonantly enhanced.

Since the interfacial electric field E$_0$ influences the observed SH signal over a timescale of minutes, it is assumed that it remains nearly constant throughout the irradiation process. This implies that neutralization of the positively charged interface states by photo-excited electrons (which would change the interfacial electric field E$_0$) plays no significant role in the observed SH signal.

Summary and conclusions

This results contained within this study expands the knowledge base with regard to the charge transfer processes across the Si/SiO_2 interface in the case of natively oxidized highly boron doped p^+-type Si. The dynamical processes involved in defect generation and charge trapping at the p^+-type Si/SiO_2 interface were investigated by means of second harmonic (SH) generation.

The SH generated signal from highly boron doped p^+-type Si/SiO_2 is interesting since it originates from a narrow region (the Si/SiO_2 interface) where a strong electric field exists across the region as a result of ionization of naturally occurring defect states at the interface. The ionization occurs as a result of the high concentration of dopants in the bulk Si. This built-in electric fields contributes an additional polarization to the medium which influences the generated SH signal significantly, yielding a strong initial SH response.

By irradiating the p^+-type Si/SiO_2 with high intensity near infra red (NIR) femtosecond laser pulses additional photo-induced defects are created near the interface. These photo-induced defects act as trap sites for both electrons and holes. Electrons are transported via a three-photon process from the Si valence band into these trap sites. Holes are transported via a four-photon process from the Si conduction band into trap sites at the interface.

The transport of electrons from the Si valence band into the photo-induced trap sites at the interface sets up an electric field that opposes the built-in electric field. This electron induced electric field dominates the interfacial electric field and hence the SH signal shortly after (> 20 s) the start of the irradiation process.

Since the hole transport process is a four-photon process compared to the three-photon process of electrons, it occurs on a much delayed time scale to that of the electron transport. The transport of holes into the interfacial trap sites sets up an electric field that opposes the one caused by the electrons, reducing the nett interfacial electric field.

The superposition of these three contributions to the nett interfacial elec-

tric field can be monitored by measuring the generated SH signal from the interface. This is because the three contributions occur on different time scales. The built-in doping induced electric field is present from the start of the irradiation and is assumed constant throughout the irradiation process. The electron induced electric field increases in strength with irradiation time, starting from zero, until an equilibrium state is reached. This occurs over a couple of minutes. Although the hole induced electric field also increases in strength from the start of the irradiation process, because it is so much slower than that of the electron induced electric field, the effect only becomes apparent after the electron induced field has reached an equilibrium value ($>$ 5 min).

By stopping the irradiation process for long enough periods to allow for the diffusion of electrons and holes from the photo-induced trap sites back into the Si valence- and conduction bands respectively, it is possible to examine the effect that pre-existing photo-induced trap sites have on the charge transfer processes. The pre-existence of these photo-induced trap sites results in accelerated charge transfer, for both electrons and holes. These accelerated dynamics are however slower than the experimental resolution of the experiment, which is in contrast to similar observations that were made in the case of undoped Si/SiO_2. Direct population mechanisms due to the proximity and density of trap sites are held responsible for the accelerated dynamics.

Since the doping induced interfacial electric field and the electron induced electric field have opposite signs, the induced effective second order polarization is different for these two fields. This is due to the tensorial nature of the third order optical susceptibility which governs electric field induced second harmonic (EFISH) generation. This effect of electric field sign reversal was investigated by measuring the rotational anisotropy pattern of both the initial SH signal, when the built-in electric field dominates, and the equilibrium SH signal, when the electron induced electric field dominates. These two rotational anisotropy patterns both show a 4-fold symmetry but with a relative 45° phase shift in the anisotropy pattern between them. This 45° phase shift has been shown, in the case of externally applied electric fields, to be an indication of electric field sign reversal across the Si/SiO_2 interface. The observed 45° phase shift is therefore taken as confirmation of the electric field sign reversal and as verification of the model used to explain the observed time dependent SH traces.

Furthermore, since the wavelength employed to perform the time-dependent SH traces lies close to a two-photon absorption resonance within the bulk Si, a large number of electron-hole pairs are generated within the Si due to two-photon absorption. These electron-hole pairs separate because of the

presence of the interfacial electric field, and effectively screen the interfacial electric field. This screening of the interfacial electric field results in an apparent deviation from the quadratic dependence of the strength of the initial SH signal on the incident intensity. This deviation from quadratic dependence is stronger the closer to the resonance the measurement is performed. This explanation was probed my measuring the dependence of the initial SH signal on the incident intensity for different wavelengths. It was found that the strongest deviation from the expected quadratic dependence occurs exactly on the two-photon resonance wavelength, confirming the explanation used for the observed results.

These results highlight the amount of research that still needs to be done regarding the defect generation and charge transfer processes at the Si/SiO_2 interface. It is clear from these results that no clear picture yet exists to explain all the observed phenomena regarding defect generation and charge transfer at this interface, especially in the case of pre-irradiated samples. It is based on the results contained within this dissertation, as well as work done earlier, that a number of questions and ideas for further experimental and numerical investigations of the Si/SiO_2 system, are brought forward.

The temporal evolution of the SH signal from pre-irradiated natively oxidized p^+-type Si/SiO_2 is accurately reproduced by a simple four exponential model. The time constants extracted from this model still needs physical interpretation. Further numerical investigations might yield insight into the exact processes responsible for the charge separation across the interface in this case.

A further investigation into the nature of the photo-induced defects could be made by annealing the samples after irradiation. This will investigate whether it is possible to remove the defects by heat treatment. An accelerated SH response from the pre-irradiated spots would indicate that the defects are still present, while the standard SH response, observed for virgin samples, would indicate that the defects have been baked out.

The observed EFISH signal is in essence a bulk effect, since the interfacial electric field induced an effective polarization in the bulk Si. By examining the EFISH signal for thin layers of oxidized Si, insight might be gained into the role of the bulk Si in the generated EFISH signal. The use of sufficiently thin Si layers may allow for the investigation of the EFISH signal in transmission, which may yield even further information.

The defect generation process is also not fully understood. This could be further investigated by generating the interface defects by a different means than the multi-photon processes employed in this study. One such method would be to use a single photon technique, which implies a laser source with photon energies in the vacuum ultraviolet.

Lastly, it might be interesting to see whether the same defect generation and charge separation that occurs in Si/SiO_2 under femtosecond irradiation, will also occur in a similar system, namely Ge/GeO_2. By comparing results for this system to that of Si/SiO_2 further insight into the processes involved in defect generation and charge separation may be gained.

Overall, the results obtained within this work stimulate further investigations into the field of buried solid-solid interfaces, in particular the Si/SiO_2 system, using SHG. This may lead to an improvement in the construction of technologically important MOS devices which could lead to enhanced consumer electronic products.

Bibliography

[1] M. Göppert-Mayer, Ann. Phys. (Leipzig) **9**, 273 (1931).

[2] P. Franken, A. Hill, C. Peters, and G. Weinrich, Phys. Rev. Lett. **7**, 118 (1961).

[3] J. A. Armstrong, N. Bloembergen, J. Ducuing, and P. S. Pershan, Phys. Rev. **127**, 1918 (1962).

[4] N. Bloembergen and P. S. Pershan, Phys. Rev. **128**, 606 (1962).

[5] G. Lüpke, Surf. Sci. Rep. **35**, 75 (1999).

[6] C. T. Williams and D. A. Beattie, Surf. Sci. **500**, 545 (2002).

[7] P. S. Winokur, H. E. Boesch, J. M. McGarrity, and F. B. McLean, J. Appl. Phys. **50**, 3492 (1979).

[8] Y. R. Shen, *The Principles of Nonlinear Optics* (Wiley, New York, 1984).

[9] F. Brown, R. E. Parks, and A. M. Sleeper, Phys. Rev. Lett. **14**, 1029 (1965).

[10] Z.-Y. Lu, C. J. Nicklaw, D. M. Fleetwood, R. D. Schrimpf, and S. T. Pantelides, Phys. Rev. Lett. **89**, 285505 (2002).

[11] T. Scheidt, Ph.D. thesis, Friedrich-Schiller-Universität, Jena (2005).

[12] S. Bergfeld, B. Braunschweig, and W. Daum, Phys. Rev. Lett. **93**, 097402 (2004).

[13] B. S. Mendoza, M. Palummo, G. Onida, and R. Del-Sole, Phys. Rev. B **63**, 205406 (2001).

[14] D. J. DiMaria and J. W. Stasiak, J. Appl. Phys. **65**, 2342 (1989).

[15] G. J. Hu and W. C. Johnson, J. Appl. Phys. **54**, 1441 (1983).

[16] F. B. McLean, IEEE Trans. Nucl. Sci. **27**, 1651 (1980).

[17] N. S. Saks, C. M. Dozier, and D. B. Brown, IEEE Trans. Nucl. Sci. **35**, 1168 (1988).

[18] P. M. Lenahan and P. V. Dressendorfer, Appl. Phys. Lett. **44**, 96 (1984).

[19] P. M. Lenahan and P. V. Dressendorfer, J. Appl. Phys. **55**, 3495 (1984).

[20] B. Kaczer, Z. Meng, and J. P. Pelz, Phys. Rev. Lett. **77**, 91 (1996).

[21] S. L. Elliott, R. F. Broom, and C. J. Humphreys, J. Appl. Phys. **91**, 9116 (2002).

[22] H. Watanabe, K. Fujita, and M. Ichikawa, Appl. Phys. Lett. **72**, 1987 (1998).

[23] H. W. K. Tom, T. F. Heinz, and Y. R. Shen, Phys. Rev. Lett. **51**, 1983 (1983).

[24] J. E. Sipe, D. J. Moss, and H. M. van Driel, Phys. Rev. B **35**, 1129 (1987).

[25] J. E. Sipe, V. Mizrahi, and G. I. Stegeman, Phys. Rev. B **35**, 9091 (1987).

[26] J. E. Sipe, J. Opt. Soc. Am. B **4**, 481 (1987).

[27] J. E. Sipe, Surf. Sci. **105**, 489 (1980).

[28] P. Guyot-Sionnest, W. Chen, and Y. R. Shen, Phys. Rev. B **33**, 8254 (1986).

[29] P. Guyot-Sionnest and Y. R. Shen, Phys. Rev. B **35**, 4420 (1987).

[30] P. Guyot-Sionnest and Y. R. Shen, Phys. Rev. B **38**, 7985 (1988).

[31] D. J. Bottomley, G. Lüpke, C. Meyer, and Y. Makita, Opt. Lett. **20**, 453 (1995).

[32] D. J. Bottomley, G. Lüpke, J. G. Mihaychuk, and H. M. van Driel, J. Appl. Phys. **74**, 6072 (1993).

[33] G. Lüpke, D. J. Bottomley, and H. M. van Driel, J. Opt. Soc. Am. B **11**, 33 (1994).

[34] D. Epperlein, B. Dick, and G. Marowsky, Appl. Phys. B **44**, 5 (1987).

[35] B. U. Felderhof and G. Marowsky, Appl. Phys. B **44**, 11 (1987).

[36] B. U. Felderhof, A. Bratz, G. Marowsky, O. Roders, and F. Sieverdes, J. Opt. Soc. Am. B **10**, 1824 (1993).

[37] F. Sieverdes, M. Pinnow, and G. Marowsky, Appl. Phys. B **54**, 95 (1992).

[38] A. Liebsch, Surf. Sci. **307-309**, 1007 (1994).

[39] B. Koopmans, F. van der Woude, and G. A. Sawatzky, Phys. Rev. B **46**, 12780 (1992).

[40] T. F. Heinz, M. M. T. Loy, and W. A. Thompson, J. Vac. Sci. Technol. B **3**, 1467 (1985).

[41] P. Bratu, K. L. Kompa, and U. Höfer, Phys. Rev. B **49**, 14070 (1994).

[42] A. A. Shklyaev and T. Suzuki, Phys. Rev. Lett. **75**, 272 (1995).

[43] C. W. van Hasselt, E. Mateman, M. A. C. Devillers, T. Rasing, A. A. Fedyanin, E. D. Mishina, O. A. Aktsipetrov, and J. C. Jans, Surf. Sci. **331-333**, 1367 (1995).

[44] O. A. Aktsipetrov, A. A. Fedyanin, E. D. Mishina, A. A. Nikulin, A. N. Rubtsov, C. W. van Hasselt, M. A. C. Devillers, and T. Rasing, Phys. Rev. Lett. **78**, 46 (1997).

[45] S. A. Mitchell, R. Boukherroub, and S. Anderson, J. Phys. Chem. B **104**, 7668 (2000).

[46] S. A. Mitchell, M. Mehendale, D. M. Villeneuve, and R. Boukherroub, Surf. Sci. **488**, 367 (2001).

[47] S. A. Mitchell, J. Phys. Chem. B **107**, 9388 (2003).

[48] R. Carriles, J. Kwon, Y. Q. An, J. C. Miller, M. C. Downer, J. Price, and A. C. Diebold, APPLIED PHYSICS LETTERS **88**, 161120 (2006).

[49] C. H. Bjorkman, T. Yasuda, C. E. Shearon, Y. Ma, G. Lucovsky, U. Emmerichs, C. Meyer, K. Leo, and H. Kurz, J. Vac. Sci. Technol. B **11**, 1521 (1993).

[50] C. H. Bjorkman, C. E. Shearon, Y. Ma, T. Yasuda, G. Lukovsky, U. Emmerichs, C. Meyer, K. Leo, and H. Kurz, J. Vac. Sci. Technol. A **11**, 964 (1993).

[51] U. Emmerichs, C. Meyer, H. J. Bakker, H. Kurz, C. H. Bjorkman, C. E. Shearon, Y. Ma, T. Yasuda, Z. Jing, G. Lucovsky, et al., Phys. Rev. B **50**, 5506 (1994).

[52] F. Ito and H. Hirayama, Phys. Rev. B **50**, 11208 (1994).

[53] H. Hirayama and K. Watanabe, Phys. Rev. B **51**, 14717 (1995).

[54] H. Hirayama, F. Ito, and K. Watanabe, J. Vac. Sci. Technol. A **13**, 750 (1995).

[55] K. Watanabe, H. Hirayama, and M. Kawata, Appl. Phys. Lett. **66**, 2232 (1995).

[56] K. Watanabe, M. Kawata, E. Hasegawa, and H. Hirayama, J. Appl. Phys. **79**, 4146 (1996).

[57] K. Koh, H. Niimi, and G. Lucovsky, Surf. Coatings Technol. **98**, 1524 (1998).

[58] G. Lucovsky, J. Vac. Sci. Technol. A **16**, 356 (1998).

[59] J. Dadap, B. Doris, Q. Deng, M. Downer, J. Lowell, and A. Diebold, Appl. Phys. Lett. **64**, 2139 (1994).

[60] S. T. Cundiff, W. H. Knox, F. H. Baumann, K. W. Evans-Lutterodt, M.-T. Tang, M. L. Green, and H. M. van Driel, Appl. Phys. Lett. **70**, 1414 (1997).

[61] G. Erley and W. Daum, Phys. Rev. B **58**, 1734(R) (1998).

[62] W. Daum, H.-J. Krause, U. Reichel, and H. Ibach, Phys. Rev. Lett. **71**, 1234 (1993).

[63] C. Meyer, G. Lüpke, U. Emmerichs, F. Wolter, H. Kurz, C. H. Bjorkman, and G. Lucovsky, Phys. Rev. Lett. **74**, 3001 (1995).

[64] G. Lüpke, D. J. Bottomley, and H. M. van Driel, Phys. Rev. B **47**, 10389 (1993).

[65] C. W. van Hasselt, M. A. Verheijen, and T. Rasing, Phys. Rev. B **42**, 9263 (1990).

[66] G. Lüpke, C. Meyer, U. Emmerichs, F. Wolter, and H. Kurz, Phys. Rev. B **50**, 17292 (1994).

[67] R. Ehlert, J. Kwon, and M. C. Downer, physica status solidi (c) **5**, 2551 (2008), URL http://dx.doi.org/10.1002/pssc.200779124.

[68] Y. Q. An and S. T. Cundiff, Phys. Rev. B **67**, 193302 (2003).

[69] O. A. Aktsipetrov, T. V. Dolgova, A. A. Fedyanin, D. Schuhmacher, and G. Marowsky, Thin Solid Films **364**, 91 (2000).

[70] M. Dürr and U. Höfer, Phys. Rev. Lett. **88**, 076107 (2002).

[71] G. Lucovsky, A. Banerjee, H. Niimi, K. Koh, B. Hinds, C. Meyer, G. Lüpke, and H. Kurz, Appl. Surf. Sci. **117/118**, 202 (1997).

[72] G. Lucovsky, K. Koh, B. Chaflin, and B. Hinds, Appl. Surf. Sci. **123/124**, 490 (1998).

[73] C. Völkmann, M. Reichelt, T. Meier, S. Koch, and U. Höfer, Phys. Rev. Lett. **92**, 127405 (2004).

[74] C. H. Lee, R. K. Chang, and N. Bloembergen, Phys. Rev. Lett. **18**, 167 (1967).

[75] O. A. Aktsipetrov, A. A. Fedyanin, V. N. Golovkina, and T. V. Murzina, Opt. Lett. **19**, 1450 (1995).

[76] J. G. Mihaychuk, J. Bloch, and H. M. van Driel, Opt. Lett. **20**, 2063 (1995).

[77] J. G. Mihaychuk, N. Shamir, and H. M. van Driel, Phys. Rev. B **59**, 2164 (1999).

[78] J. Bloch, J. G. Mihaychuk, and H. M. van Driel, Phys. Rev. Lett **77**, 920 (1996).

[79] N. Shamir, J. G. Mihaychuk, and H. M. van Driel, Phys. Rev. Lett. **82**, 359 (1999).

[80] O. A. Aktsipetrov, A. A. Fedyanin, E. D. Mishina, A. N. Rubtsov, C. W. van Hasselt, M. A. C. Devillers, and T. Rasing, Phys. Rev. B **54**, 1825 (1996).

[81] O. A. Aktsipetrov, A. A. Fedyanin, E. D. Mishina, A. N. Rubtsov, C. W. van Hasselt, M. A. C. Devillers, and T. Rasing, Surf. Sci. **352-354**, 1033 (1996).

[82] T. V. Dolgova, A. A. Fedyanin, and O. A. Aktsipetrov, Phys. Rev. B **68**, 073307 (2003).

[83] J. I. Dadap, X. F. Hu, M. H. Anderson, M. C. Downer, J. K. Lowell, and O. A. Aktsipetrov, Phys. Rev. B **53**, R7607 (1996).

[84] G. Lüpke, C. Meyer, C. Ohlhoff, H. Kurz, S. Lehmann, and G. Marowsky, Opt. Lett. **20**, 1997 (1995).

[85] C. Meyer, G. Lüpke, Z. G. Lü, A. Gölz, H. Kurz, and G. Lucovsky, J. Vac. Sci. Technol. B **14**, 3107 (1996).

[86] C. Ohlhoff, G. Lüpke, C. Meyer, and H. Kurz, Phys. Rev. B **55**, 4596 (1997).

[87] P. Godefroy, W. de Jong, C. W. van Hasselt, M. A. C. Devillers, and T. Rasing, Appl. Phys. Lett. **68**, 1981 (1996).

[88] Z. Marka, R. Pasternak, S. N. Rashkeev, Y. Jiang, S. T. Pantelides, N. H. Tolk, P. K. Roy, and J. Kozub, Phys. Rev. B **67**, 045302 (2003).

[89] Z. Marka, S. K. Singh, W. Wang, S. C. Lee, J. Kavich, B. Glebov, S. N. Rashkeev, A. P. Karmarkar, R. G. Albridge, S. T. Pantelides, et al., IEEE Trans. Nucl. Sci. **47**, 2256 (2000).

[90] J. Fang, W. W. Heidbrink, and G. P. Li, J. Appl. Phys. **88**, 2641 (2000).

[91] J. Fang and G. P. Li, Appl. Phys. Lett. **72**, 1987 (1998).

[92] M. Cernusca, R. Heer, and G. A. Reider, Appl. Phys. B: Lasers and Optics **B66**, 367 (1998).

[93] G. A. Reider, M. Cernusca, and M. Hofer, Appl. Phys. B: Lasers and Optics **B68**, 343 (1999).

[94] N. Shamir, J. G. Mihaychuk, and H. M. van Driel, J. Vac. Sci. Technol. A **15**, 2081 (1997).

[95] S. A. Mitchell, S. Janz, and J. A. Bardwell, Chem. Phys. Lett. **310**, 361 (1999).

[96] V. Fomenko, C. Hurth, T. Ye, and E. Borguet, J. Appl. Phys. **91**, 4394 (2002).

[97] W. Wang, G. Lüpke, M. D. Ventra, S. T. Pantelides, J. M. Gilligan, N. H. Tolk, I. C. Kizilyalli, P. K. Roy, G. Margaritondo, and G. Lucovsky, Phys. Rev. Lett. **81**, 4224 (1998).

[98] Y. D. Glinka, W. Wang, S. K. Singh, Z. Marka, S. N. Rashkeev, Y. Shirokaya, R. Albridge, S. T. Pantelides, N. H. Tolk, and G. Lucovsky, Phys. Rev. B **65**, 193103 (2002).

[99] V. Fomenko and E. Borguet, Phys. Rev. B **68**, 081301(R) (2003).

[100] T. Scheidt, E. G. Rohwer, H. M. von Bergmann, and H. Stafast, Phys. Rev. B **69**, 165314 (2004).

[101] J. D. Jackson, *Classical Electrodynamics* (Wiley, New York, 1999).

[102] P. W. Milonni and J. H. Eberly, *Lasers* (Wiley-interscience, 1988).

[103] R. W. Boyd, *Nonlinear Optics* (Academic Press, 2003).

[104] N. Bloembergen, R. K. Chang, S. S. Jha, and C. H. Lee, Phys. Rev. B **174**, 813 (1968).

[105] P. H. Neethling, E. G. Rohwer, H. M. von Bergmann, and H. Stafast, Phys. Stat. Sol. (c) **2**, 552 (2008).

[106] I. M. Baranova and K. N. Evtyukhov, Quantum Electron **25**, 1235 (1995).

[107] P.-F. Brevet, *Surface Second Harmonic Generation* (Presses polytechniques et universitaires romandes, 1997).

[108] P. F. Moulton, J. Opt. Soc. Am. B **3**, 125 (1986).

[109] U. Morgner, F. X. Kärtner, S. H. Cho, H. A. Haus, J. G. Fujimoto, E. P. Ippen, V. Scheuer, G. Angelow, and T. Tschudi, Opt. Lett. **24**, 411 (1999).

[110] M. Nisoli, S. D. Silvestri, O. Svelto, R. Szipöcs, K. Ferencz, C. Spielmann, S. Sartania, and F. Krausz, Opt. Lett. **22**, 522 (1997).

[111] T. Brabec, C. Spielmann, P. F. Curley, and F. Krausz, Opt. Lett. **17**, 1292 (1992).

[112] O. A. Aktsipetrov, A. A. Fedyanin, A. V. Melnikov, E. D. Mishina, A. N. Rubtsov, M. H. Anderson, P. T. Wilson, H. ter Beek, X. F. Hu, J. I. Dadap, et al., Phys. Rev. B **60**, 8924 (1999).

[113] R. P. Southwell, M. A. Mendicino, and E. G. Seebauer, J. Vac. Sci. Technol. A **14**, 928 (1996).

[114] K. Dev, M. Y. L. Jung, R. Gunawan, R. D. Braatz, and E. G. Seebauer, Phys. Rev. B **68**, 195311 (2003).

[115] M. J. Keevers and M. A. Green, Solar Energy Materials and Solar Cells **41/42**, 195 (1996).

[116] M. A. Green and M. J. Keevers, Progress in Photovoltaics **3**, 189 (1995).

[117] C. V. Shank, R. Yen, and C. Hirlimann, Phys. Rev. Lett. **50**, 454 (1983).

[118] C. V. Shank, R. Yen, and C. Hirlimann, Phys. Rev. Lett. **51**, 900 (1983).

[119] J. I. Dadap, F. X. Hu, N. M. Russell, J. G. Ekerdt, J. K. Lowell, and M. C. Downer, IEEE J. Sel. Top. Quantum Electron. **1**, 1145 (1995).

[120] T. Scheidt, E. G. Rohwer, P. H. Neethling, H. M. von Bergmann, and H. Stafast, Accepted for publication in J. Appl. Phys. (2008).

[121] K. Dev and E. G. Seebauer, Surf. Sci. **550**, 185 (2004).

[122] M. McEllistrem, G. Haase, D. Chen, and R. J. Hamers, Phys. Rev. Lett. **70**, 2471 (1993).

[123] M. Y. L. Jung, R. Gunawan, R. D. Braatz, and E. G. Seebauer, J. Appl. Phys. **95**, 1134 (2004).

[124] D. E. Aspnes, Surf. Sci **37**, 418 (1973).

[125] Y. Q. An and S. T. Cundiff, Appl. Phys. Lett. **81**, 5174 (2002).

[126] J. I. Dadap, P. T. Wilson, M. H. Anderson, and M. C. Downer, Opt. Lett. **22**, 901 (1997).

[127] V. Fomenko and E. B. J.-F. Lam and, Phys. Rev. B **63**, 121316(R) (2001).